Bulletin of Physics Projects

Journal homepage: http://www.bbcphysics.in/abt-journal.html

Nanostructured ZnO and its derivatives - properties and applications

Bimal K. Sarma[#]

Department of Physics, Gauhati University

[#] **Corresponding author's e-mail address:** sarmabimal@gmail.com

Abstract

With the emergence of nanotechnology, two, one and zero- dimensional structures are of great interest as they demonstrate size dependent material properties different from their bulk counterpart. To be precise enough, properties are shape dependent as well. Nanostructured ZnO is a low cost and environmentally acceptable semiconductor with high photosensitivity, photocatalytic activity and piezoelectric properties. This topical review presents current scenario of ZnO and its derivatives – metal-semiconductor heterostructure, piezoelectric nanogenerators, and transparent conductors where well defined morphology, microstructure, and interfacial properties are crucial for specific applications.

1. Introduction:

Low dimensional structures have become materials of choice for various technological advancements primarily in the area of inorganic and organic semiconductor devices, supercapacitors, catalysis, spintronics, piezoelectric nanogenerators, and transparent conductors [1–4]. The progress have so far been encouraging but at the same time challenges are tremendous at nanoscale – a domain far from classical physics world whereas quantum effects are observed in such a *large system* with many atoms with structural disorder. Scientists have put forward that a simple scaling law for the feature size of a semiconductor chip is inadequate beyond 2020 – scaling with innovation is the best possible solution since quantum effects dominate in the sub-10 nm regime [5].

Undoubtedly, the future of semiconductors is *nanotechnology*. Nanoscale is the smallest scale (till date) where technology is available by creating exotic structures by manipulating things in the *microworld*.

This topical review presents a scientific approach related to the understanding of the properties of nanostructured ZnO and its derivatives. ZnO is a semiconductor which belongs to a promising class as being wide band gap semiconductor (direct band gap of 3.37 eV at room temperature) with large exciton binding energy 60 meV [6]. ZnO is *n*-type in its native form due to defect states and behave as a degenerate semiconductor upon heavy doping which leads to the development of transparent conductors for solar cells and flat panel displays [4]. Moreover, ZnO can function as a piezoelectric generator

and demonstrates room temperature ferromagnetism upon doping with transition elements [2, 7]. This is a technologically important semiconductor which is biocompatible, environment friendly, low cost, and highly photosensitive. The distinctive advantages of ZnO over GaN (a promising optoelectronic material) which has band gap of 3.4 eV and similar crystal structure with lattice matching to a great extent may lead to a better alternative to GaN for the light emitting devices. At nanoscale, ZnO based metal-semiconductor heterostructures are known for multifunctional behaviour – excellent plasmon-exciton driven photocatalysts when nanoparticles of Ag and Au are embedded on the surface of ZnO and potential near UV light source due to enhanced near band edge luminescence due to free exciton recombination and plasmon coupling of metal nanoparticles in proximity of the emitter [8–10]. Considering the emergence of ZnO derivatives, this review article is primarily focused on three different aspects – metal-semiconductor heterostructure, piezoelectric nanogenerator, and transparent conductor. The author has intentionally skipped elaborate discussions on many important properties of ZnO viz. defect engineering, room temperature ferromagnetism and light emission which have featured in existing review articles [1, 2, 6].

2. Growth of ZnO nanostructure:

Several growth processes exist to create ZnO nanostructures with variety in morphology – nanorods, nanowires, nanoparticles, nanobelts, nanorings, nanosprings, nanocombs and in some other less common shape. Both wet chemical and dry physical methods can be adopted – chemical processes are known for greater control over size and shape, easily scalable and inexpensive. For example, a hydrothermal growth can be carried out using zinc nitrate hexahydrate and methenamine as precursors in aqueous solution. Reactions are carried out in a glass bottle having screw cap and substrate loaded where supersaturation at a growth temperature of 90–95 °C drives the nucleation and subsequent growth of ZnO nanostructure on variety of substrates [11]. The reactions proceed as

$$(CH_2)_6 N_4 + 6H_2O \leftrightarrow 6HCHO + 4NH_3$$

$$NH_3 + H_2O \leftrightarrow NH_4^+ + OH^-$$

$$2OH^- + Zn^{2+} \rightarrow ZnO + H_2O$$
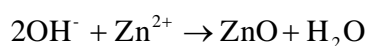
On the other hand, physical processes such as sputtering, pulsed laser deposition rely on energetic events for the growth of nanostructures and thin films known for strong adhesion suitable for fabrication of devices [12–14]. ZnO thin films are deposited using ZnO target through ion bombardment – a process known as sputtering. Magnetron sputtering is a versatile technique for the deposition of uniform thin films over a large area substrate. Usually Argon gas is used which is weakly ionized at low pressure, creates a plasma, allowing Ar ions to bombard the target surface to liberate target atoms from the surface [12]. A detailed review on the growth of ZnO nanostructures is presented in ref. [2].

3. ZnO based metal-semiconductor heterostructure:

A metal-semiconductor interface involving nanostructured ZnO and metal nanoparticles such as Ag, Au, and Al can enhance the light-matter interaction due to coupling of surface plasmons of metal nanoparticles with quantum states of excitons through long range Coulomb interaction. This is vital in understanding interface physics that can lead to the design of light emitting devices, photodetectors, solar cells and sensors. ZnO is an excellent photocatalyst although limited works are reported compared to TiO_2 [15–17]. However, both TiO_2 and ZnO possess photocatalytic activity only when excited by UV light (requirement arises due to wide band gap of these materials). A novel approach is narrowing of the band gap which leads to the red shift of the onset of fundamental absorption allowing photoexcitation by light with low photon energy. This is an emerging field where defect engineered band gaps are vital for visible light absorption (major content of solar spectrum). The narrowing of band gaps in nanostructured ZnO is primarily decided by the overlap of non-localized states due to oxygen vacancies with the valence band edge [14]. Accordingly, in a ZnO with a handful of oxygen vacancies the valence band edge is raised in the gap region making the band gap narrower as compared to defect free semiconductor. Noble metals, Ag and Au in particular at nanoscale are well known for their ability to absorb visible light due to surface plasmon excitation which is dependent on several parameters including size and shape (morphology), inter-particle separation, and dielectric constant of the surrounding medium [18, 19]. Light absorption in the visible region can be enhanced strongly by creating metal-semiconductor interface (nanometer and sub-nanometer regime) by a way of fabricating such structures with metal nanoparticles loaded on the semiconductor surface. Figure 1 shows field

emission scanning electron microscopy (FE-SEM) images of Ag/ZnO heterostructure using PET and Si wafer as substrates. The hydrothermal growth of ZnO is adopted which is inexpensive and easily scalable for large scale production [8].
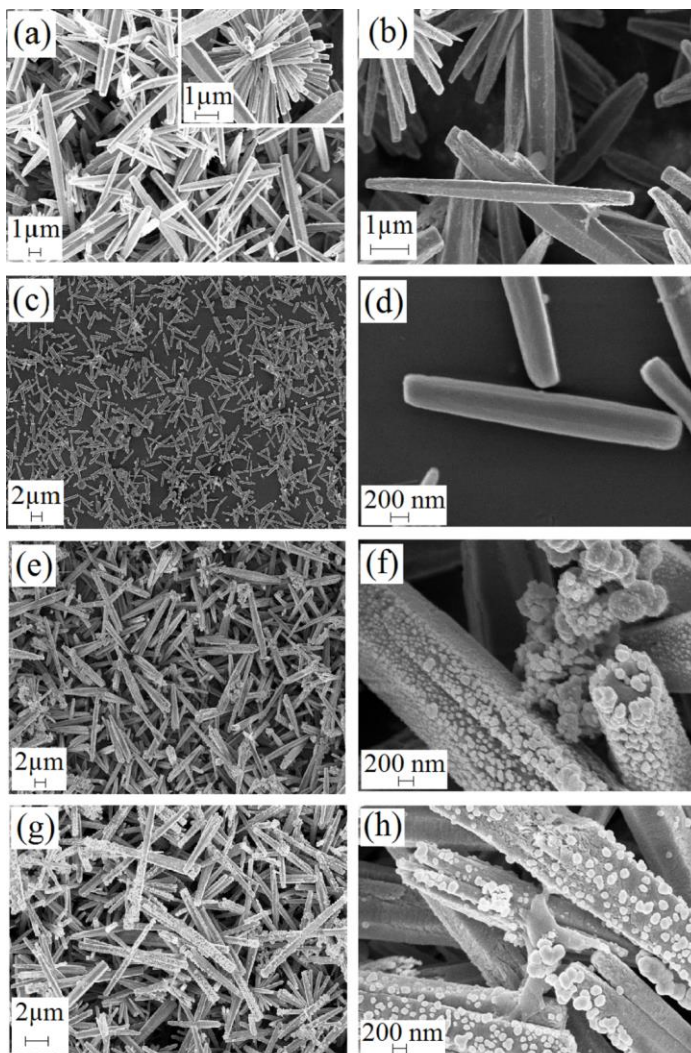
Figure 1: FE-SEM images of (a) ZnO microrods on PET with 10 mM solute concentration. The inset demonstrates the flowerlike pattern of ZnO microrods, (b) higher magnification image of ZnO microrods, (c) ZnO microrods on PET with 1mM solute concentration, (d) higher magnification image of near monodispersed ZnO microrods, (e) Ag/ZnO heterostructure deposited on PET with 10 mM solute concentration for ZnO, (f) higher magnification image of Ag/ZnO heterostructure deposited on PET, (g) Ag/ZnO heterostructure deposited on silicon wafer with 10 mM solute concentration for ZnO and (h) higher magnification image of Ag/ZnO heterostructure deposited on silicon wafer. Reproduced with permission from ref. [8] ©Elsevier
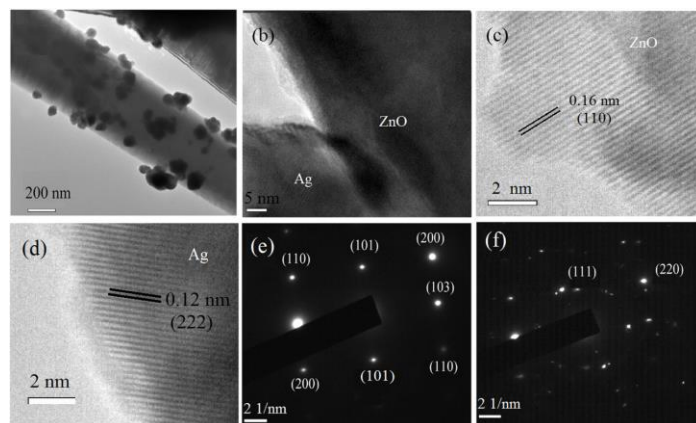
Figure 2: (a) TEM image of Ag/ZnO heterostructure deposited on silicon wafer with 10 mM solute concentration for ZnO, (b) High resolution TEM (HRTEM) image of a ZnO microrod and an Ag nanoparticle showing the attachment, (c) HRTEM image of ZnO microrod showing lattice spacing for (110) plane, (d) HRTEM image of Ag nanoparticle showing lattice spacing for (222) plane, (e) Selected area electron diffraction (SAED) pattern of ZnO microrod and (d) SAED pattern of Ag nanoparticle. Reproduced with permission from ref. [8] ©Elsevier

The fabrication of Ag/ZnO heterostructure is carried out by allowing photo-deposition of Ag on the surface of ZnO [8]. From figure 1 it is clear that dense arrangement of ZnO microrods is evident at a higher solute concentration. At a lower solute concentration, the arrangement of ZnO microrods become less dense, and rods have lower aspect ratio. Interestingly, these microrods constitute a near monodispersity in size and shape. In the Ag/ZnO heterostructure, spherical Ag nanoparticles are in direct attachment on the different facets of ZnO microrods. In several situations, ZnO microrods are decorated with Ag nanoparticles up to the ends of the rods (figure 1f). Transmission electron microscopy (TEM) images reveal the formation of Ag/ZnO interface. ZnO microrods are single crystalline (figure 2e) and Ag nanoparticles have polycrystalline features as confirmed by the ring like pattern in the selected area electron diffraction (SAED). It is worthy to note that the optical reflectance spectra of Ag/ZnO heterostructure (figure not shown here) demonstrate broad surface plasmon resonance (SPR) due to Ag nanoparticles around 445 nm [8]. This plasmonic feature enhances light absorption in the visible region which may lead to better photocatalytic activity of Ag/ZnO heterostructure compared with that of ZnO alone. Photoluminescence (PL) spectra (figure 3a) of ZnO

microrods have the features of near band emission (390 nm) due to recombination of free excitons and prominent visible emission due to defects. The luminescence is quenched to a great extent in case of Ag/ZnO heterostructure which is an indicative of the fact that interfacial charge transfer hinders electron-hole recombination in a significant way. However, quenching of PL (especially defect driven PL) is limited in the case of Ag/ZnO heterostructure grown over Si wafer due lower surface coverage of ZnO microrods by Ag nanoparticles (figure 3c).
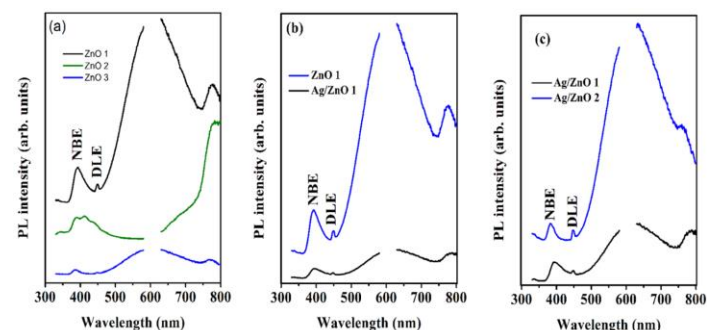
Figure 3: PL spectra of (a) ZnO microrods deposited on PET with 10 mM solute concentration (ZnO 1), ZnO microrods deposited on PET with 1 mM solute concentration (ZnO 2) and ZnO microrods deposited on silicon wafer with 10 mM solute concentration (ZnO 3), (b) ZnO 1 and Ag/ZnO heterostructure deposited on PET with 10 mM solute concentration for ZnO (Ag/ZnO 1), and (c) Ag/ZnO 1 and Ag/ZnO heterostructure deposited on silicon wafer with 10 mM solute concentration for ZnO (Ag/ZnO 2). The discontinuities in the PL spectra (580–630 nm) are to avoid the expected first harmonic of the excitation wavelength. Reproduced with permission from ref. [8] ©Elsevier

The schematic of energy level diagram for ZnO microrods with a band gap of 3.10 eV with probable defect states consistent with PL results are depicted in figure 4a. Upon photoexcitation of Ag/ZnO heterostructure, surface plasmon excitation allows transfer of electrons to the conduction band of ZnO as shown in figure 4b. In the subsequent time, electrons are transferred back to Ag nanoparticles which are in direct contact with ZnO microrods. An efficient direct electron transfer between Ag nanoparticles and ZnO microrods through the metal-semiconductor interface leads to the quenching of PL in Ag/ZnO heterostructure [8]. Meanwhile, electrons can transfer to defect states of ZnO. An efficient charge

separation and enhanced light-matter interaction is decisive for better photocatalytic activity of Ag/ZnO heterostructure in contrast to slower degradation rate of methyl orange by ZnO alone [8]. Such variations are presented in figure 5. The photocatalysis is carried out using 3 cm × 3 cm film and irradiating with two 11 W tube lights (TUV11W Philips).
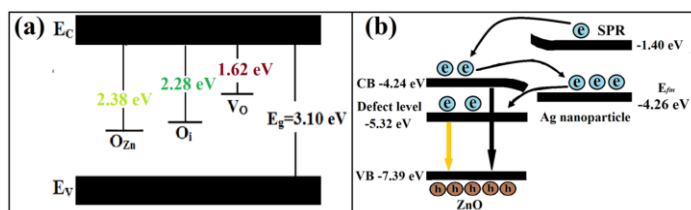
Figure 4: Schematic energy level diagram (a) for the defect states in the wide green PL band of ZnO, (b) showing PL quenching in Ag/ZnO heterostructure. The position of the valence band (VB) of ZnO and the Fermi level of Ag are taken from the ref. [20]. Reproduced with permission from ref. [8] ©Elsevier
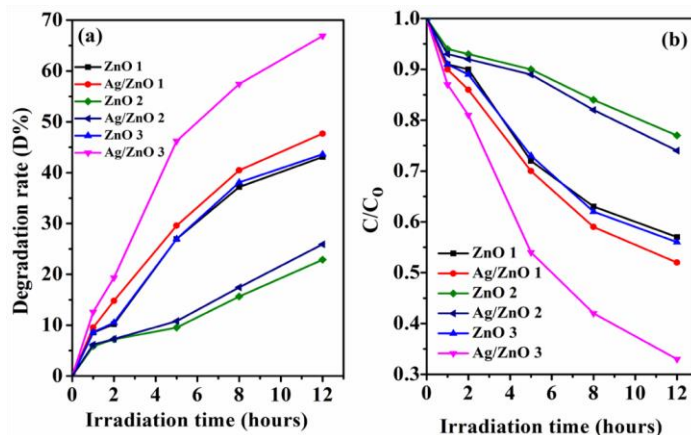
Figure 5: (a) Plots of degradation rate of MO versus irradiation time with ZnO microrods prepared with 10 mM solute concentration on PET (ZnO 1), Ag/ZnO heterostructure on PET with 10 mM solute concentration for ZnO (Ag/ZnO 1), ZnO microrods prepared with 1 mM solute concentration on PET (ZnO 2), Ag/ZnO heterostructure on PET with 1 mM solute concentration for ZnO (Ag/ZnO 2), ZnO microrods prepared with 10 mM solute concentration on silicon wafer (ZnO 3), Ag/ZnO heterostructure on silicon wafer with 10 mM solute concentration for ZnO (Ag/ZnO 3) as catalysts, (b) Plots of the normalized concentration of MO versus irradiation time with ZnO 1, Ag/ZnO 1, ZnO 2, Ag/ZnO 2, ZnO 3 and Ag/ZnO3 as catalysts. Reproduced with permission from ref. [8] ©Elsevier

Plasmon mediated and plasmon enhanced light absorption in semiconductor heterostructures have been crucial in the design of light extraction and light harvesting devices. The topic discussed above is mere an example. Recent progresses have been tremendous in this exciting field, if realized as expected will take the centre stage for the development of highly efficient photocatalysts and next generation light emitting and photovoltaic devices.

4. Piezoelectric nanogenerators:

ZnO is a unique choice as it demonstrates both semiconducting and piezoelectric properties at the same time. Nanostructured ZnO has the ability to convert mechanical energy to electric power [2, 7]. At nanoscale, ZnO can be integrated to develop self-powered nanodevices which harvest energy from the environment. Vertically aligned ZnO nanowires are useful for this purpose as these one dimensional (1D) structures can be applied successfully for transport of charge carrier in a
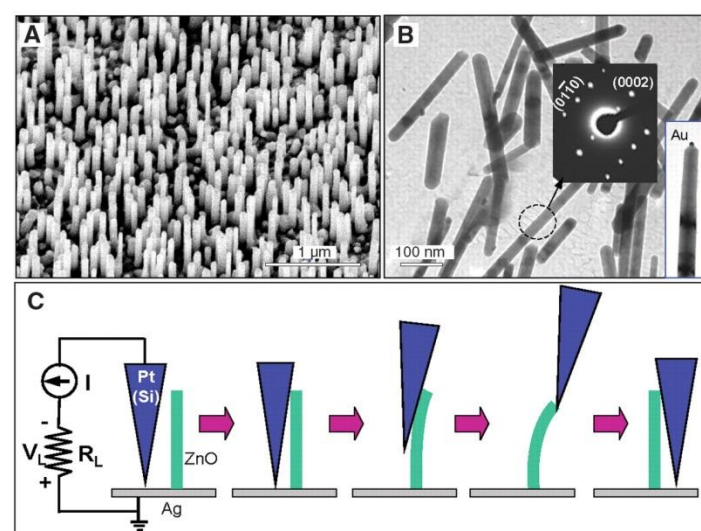
Figure 6: (A) Scanning electron microscopy images of vertically aligned ZnO nanowires grown on α-Al$_2$O$_3$ substrate, (B) Transmission electron microscopy images of ZnO nanowires showing the typical structure without an Au particle or with a small Au particle at the top. Inset at center: an electron diffraction pattern of ZnO nanowire. Inset at right: image of a ZnO nanowire with an Au nanoparticle. (C) Experimental arrangement for generating electricity by deforming a nanowire with a conductive AFM tip. The base of the nanowire is grounded and an external load of R_L is applied, which is much larger than the resistance R_I of the nanowire. The AFM scans across the nanowire arrays in contact mode. Reproduced with permission from ref. [7]. ©AAAS

particular direction. Wang and Song [7] conducted a study on the growth of aligned nanowires grown on α-Al$_2$O$_3$ substrate using Au as the catalyst (figure 6). ZnO nanowires are vertically aligned, single crystalline and having uniform shape. ZnO nanowires are grown along [001] direction and the nanowire assembly is less dense and short such that the tip of the AFM (Si tip coated with Pt film) can reach one nanowire without touching another. The tip is scanned over the top of ZnO nanowires and the AFM is operated in the contact mode with a constant force of 5 nN between the tip and the sample surface. A conductive silver paste is used as the bottom contact and the output voltage across a load resistance R_L (500 MΩ) is measured as the tip is scanned over the sample surface. As the tip is scanned, the nanowires are bent and the bending is recorded directly in the topography. In figure 7, many sharp peaks for the output voltage V_L can be seen. Interestingly, the locations of the voltage peaks are the sites of ZnO nanowires. It is clear from the figure 7 that the piezoelectricity is detected when the deflection of nanowires approaches its maximum. When a nanowire is released, V_L drops to the noise level. The damping of the voltage peak can be qualitatively explained with the help of an equivalent circuit as shown in figure 7E. The full width at half maximum of a voltage peak is estimated to be ~ 0.6 ms. In the equivalent circuit, a ZnO nanowire is considered as a resistor R_I and a capacitor C. The life time of the output voltage is $(R_L+R_I)/C$. R_I being negligibly small compared to the load resistance R_L, the equivalent capacitance of the nanowire and the system is $C \approx 1.2$ pF.

The efficiency of the electrical power generated by this process is achieved upto 17–30% which is quite high possibly due to the extremely large deformation that is sustained by 1D ZnO structure. The underlying physical principle for the generation of piezoelectric energy is how the semiconducting properties are coupled with the piezoelectric properties. The process of piezoelectric power generation using 1D ZnO based nanogenerators is illustrated in figure 8 where transport is governed by the metal-semiconductor Schottky barrier due to higher work function of Pt (6.1 eV) compared to electron affinity of ZnO (4.5 eV). This work has opened up avenue for the self-powered devices which generates electricity from the mechanical energy available in the environment such as human body where implantable biomedical device should work without external power.

FEATURED ARTICLE
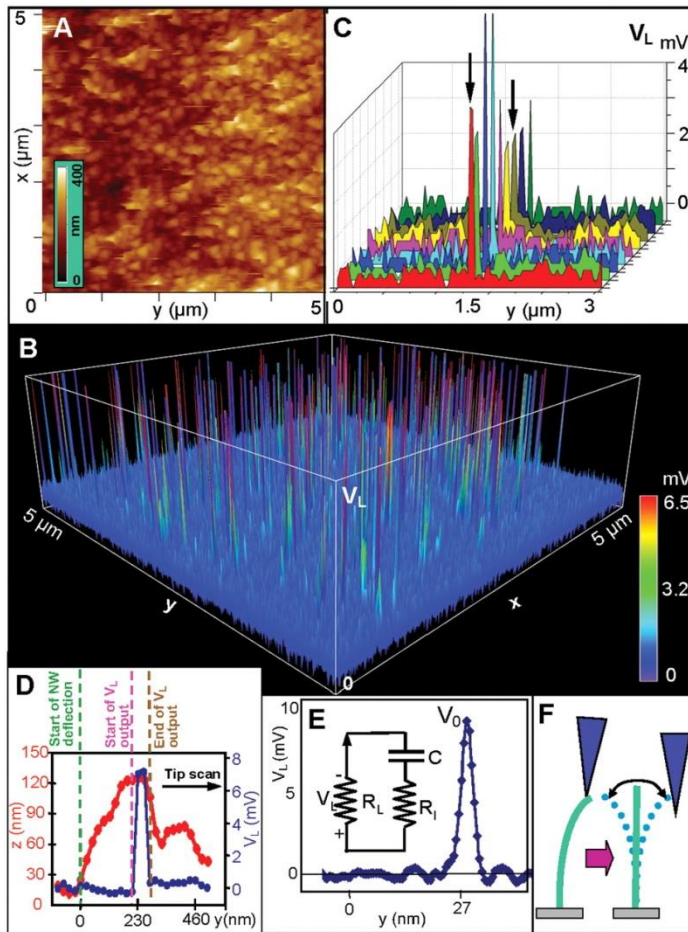
Figure 7: Topography (A) and corresponding output voltage image (B) of ZnO nanowire arrays. (C) A series of line profiles of the voltage output signal when the AFM tip scanned across a vertical nanowire at a time interval of 1 min. Colours represent the outputs required for a series of scans. (D) Line profiles from the topography (red) and output voltage (blue) images across a nanowire. (E) Line profile of the voltage output signal when the AFM tip scans across a vertical nanowire. The time spent to acquire and output one scan point was 0.05 ms, which was achieved at the maximum scan frequency of the AFM. The inset is an equivalent circuit of the measurement to be used for simulating the discharging process. (F) The resonance vibration of a nanowire after being released by the AFM tip, showing that the stored elastic energy is transferred mainly into vibrational energy. Reproduced with permission from ref. [7]. ©AAAS

5. Transparent conductor:

One of the most fascinating properties of ZnO derivatives is its ability to conduct electricity just like metals but remain transparent to light unlike metals. Tin doped indium oxide (Sn:In$_2$O$_3$) commonly known as ITO (indium tin oxide) is widely used owing to its excellent transparency and low resistivity.
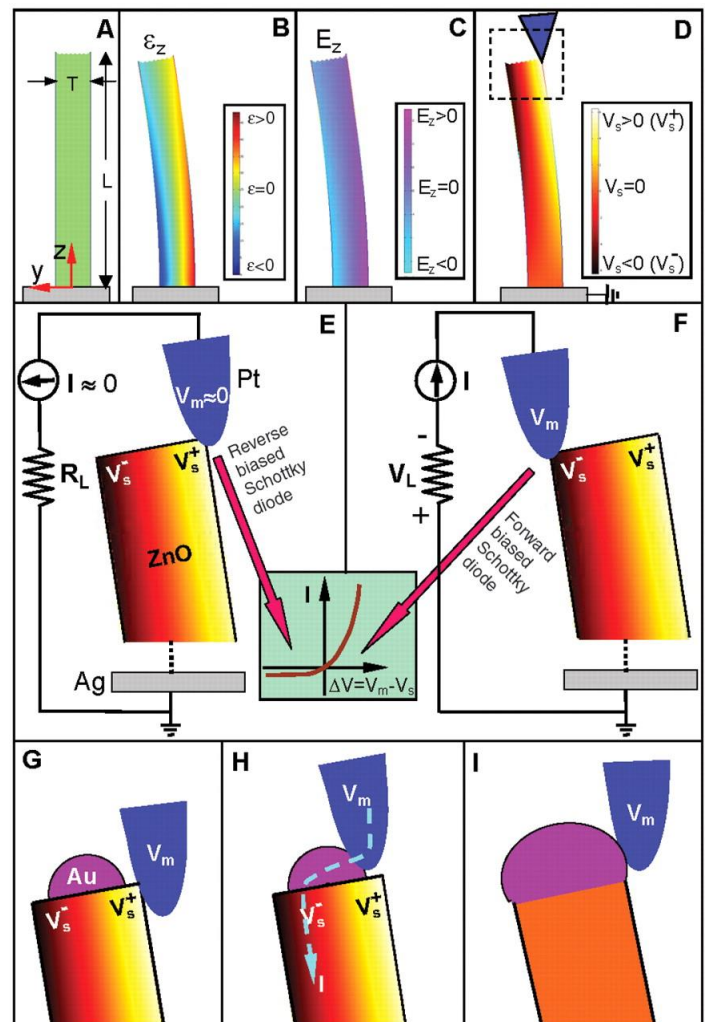
Figure 8: (A) Schematic definition of a nanowire and the coordination system. (B) Longitudinal strain ε_z distribution in the nanowire after being deflected by an AFM tip from the side. (C) The corresponding longitudinal piezoelectric induced electric field E_z distribution in the nanowire. (D) Potential distribution in the nanowire as a result of the piezoelectric effect. (E and F) Contacts between the AFM tip and the semiconductor ZnO nanowire [boxed area in (D)] at two reversed local contact potentials (positive and negative), showing reverse- and forward-biased Schottky rectifying behavior. The inset shows a typical current-voltage (I-V) relation characteristic of a metal-semiconductor (n-type) Schottky barrier. (G and H) Contact of the metal tip with a ZnO nanowire with a small Au particle at the top. (I) Contact of the metal tip with a ZnO nanowire with a large Au particle at the top. Reproduced with permission from ref. [7]. ©AAAS

Toxicity and scarcity of indium have been always an issue which triggers search for better alternatives of ITO as transparent conductors in optoelectronic devices. Figure 9

shows schematic of a typical multilayer structure based on two ZnO layers with an intermediate Ag thin layer [21].
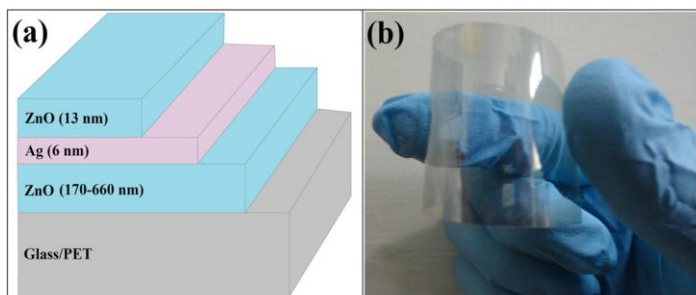
Figure 9: (a) A schematic of ZnO/Ag/ZnO multilayer transparent conductors deposited on glass and PET substrates by magnetron sputtering and (b) photograph of a flexible ZnO/Ag/ZnO transparent conductor. Reproduced with permission from ref. [21] ©Elsevier

These multilayer transparent conductors using nanocrystalline ZnO thin films have been realized with deposition conditions summarized in Table 1. These films are transparent and conducting so it is interesting to understand the electro-optical properties and their dependence on the structural properties of ZnO layers. The performance of a multilayer transparent conductor is usually attributed to the optimum thickness of the intermediate layer – the higher the thickness the better the electrical conductivity. However, a thick metal layer can drastically reduce the optical clarity. Considering an optimal thickness of mid- Ag layer (6 nm), ZnO/Ag/ZnO multilayer structures are grown with different thickness of the bottom ZnO layer.

Table I: Deposition conditions of ZnO/Ag/ZnO multilayer transparent conductors

Sample code	Multilayer structures	Deposition conditions for ZnO bottom layer		
		Sputtering power (W)	Deposition time (min)	Thickness (nm)
A	PET/ZnO/Ag/ZnO	35	30	170
B	PET/ZnO/Ag/ZnO	70	30	340
C	PET/ZnO/Ag/ZnO	50	60	330
D	PET/ZnO/Ag/ZnO	70	60	462
E	Glass/ZnO/Ag/ZnO	35	30	170
F	Glass/ZnO/Ag/ZnO	50	30	242
G	Glass/ZnO/Ag/ZnO	100	60	660

* reproduced with permission ref. [21] ©Elsevier

X-ray diffraction (XRD) experiments under grazing incidence suggest formation of wurtzite phase of ZnO with preferred orientation along c–direction. The formation of nanocrystalline Ag thin films between two ZnO layers is confirmed by the appearance of a weak diffraction peak at a diffraction angle of 38.15° corresponding to (111) reflection plane of Ag which has f.c.c structure. The indexing of diffraction peaks of textured ZnO and nanosized Ag thin films are carried out using the International Centre for Diffraction Data (ICDD) files 36-1451 and 4-0783 respectively. The diffraction patterns of ZnO/Ag/ZnO multilayer films are shown in Figure 10.
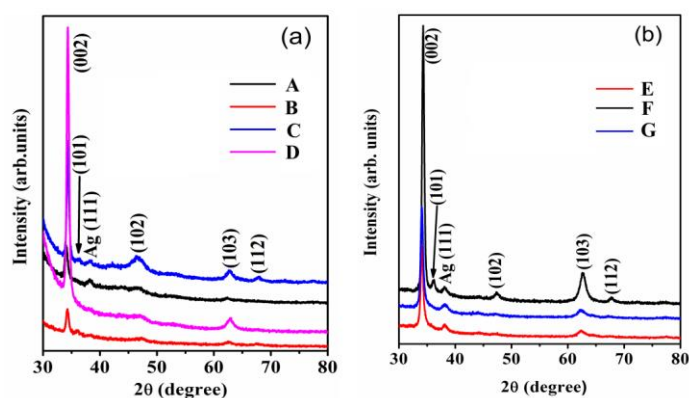
Figure 10: XRD patterns of ZnO/Ag/ZnO multilayer transparent conductors deposited on (a) PET and (b) glass substrates. Reproduced with permission from ref. [21] ©Elsevier
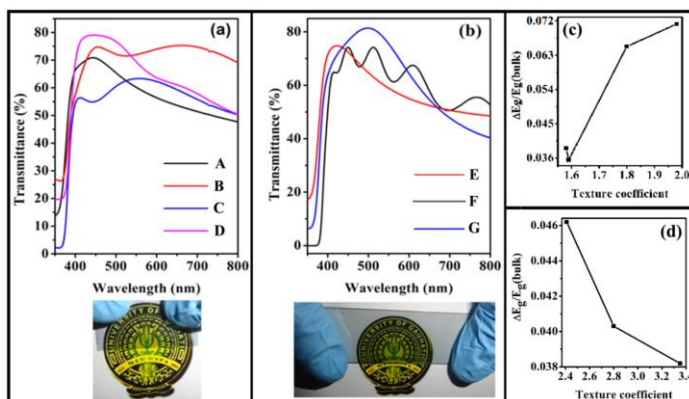
Figure 11: UV-Vis transmittance spectra of ZnO/Ag/ZnO multilayer transparent conductors deposited on (a) PET and (b) glass substrates. Representative photographs of films are also shown. Fractional change of band gap with texture of ZnO nanocrystals in multilayer films deposited on (c) PET and (d) glass. Reproduced with permission from ref. [21] ©Elsevier

Multilayers films possess reasonably good visible light transparency as suggested by transmittance spectra as

shown in Figure 11. A significant drop of transmittance below 400 nm is attributed to the fundamental absorption in ZnO when photon energy is close to the band gap (which is determined in the range 3.23–3.28 eV). In general, band gaps of low dimensional semiconductors widen primarily due to quantum confinement of electrons and holes and this phenomenon is commonly observed as the blue shift of absorption spectrum compared to that of the bulk semiconductor of the same material. Surprisingly, band gaps of ZnO/Ag/ZnO multilayer thin films become narrow (the band gap of bulk ZnO is 3.37 eV at room temperature) which could be attributed to various defects in ZnO and primarily to the non-localized oxygen vacancies near the valence band edge in the gap region [14]. However, the effect of texture is excluded as a possible reason behind the observed red shift of absorption edge (see figure 11).

electrons from Ag can be transferred to ZnO through Ag/ZnO interface as shown in Figure 4. This is how the flow of electrons can lead to high sheet carrier density of ZnO/Ag/ZnO multilayer transparent conductor.
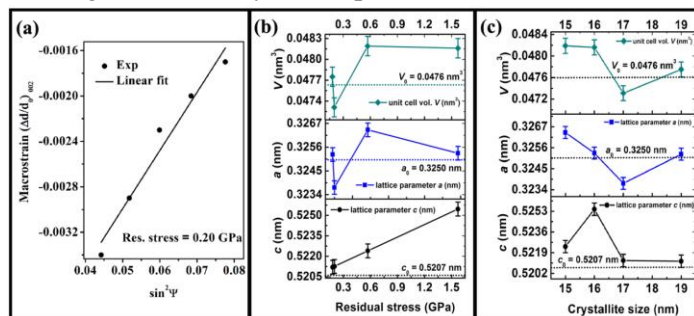
Figure 13: (a) A typical $\sin^2(\Psi)$ plot for the determination of residual stress of ZnO nanocrystals in ZnO/Ag/ZnO multilayer thin films with bottom ZnO layer sputtered at 70 W for 60 min on PET. Variations of the lattice parameters a, c and unit cell volume V for ZnO in ZnO/Ag/ZnO multilayer thin films on PET with (b) residual stress and (c) crystallite size. Reproduced with permission from ref. [21] ©Elsevier

Figure 12: Schematic energy level diagrams of bottom ZnO layer, mid Ag layer, and top ZnO layer, (a) before contact and (b) after contact. The position of the valence band (VB) of ZnO is taken from the ref. [20]. Reproduced with permission from ref. [21] ©Elsevier

The co-existence of good optical transmittance and low sheet resistance is an essential requirement of a transparent conductor and which is possible using ZnO/Ag/ZnO multilayer thin films. Clearly Sample D and Sample G (Table2) display better figure of merit. The work function of Ag is lower than that of ZnO. In the process of fabrication of ZnO/Ag/ZnO multilayer structure, the mid Ag layer is brought in contact with two ZnO layers and

Figure 14: Variations of sheet resistance (R_{Sh}), transmittance (T) and figure of merit (φ_{TC}) for ZnO/Ag/ZnO multilayer thin films on PET with (a) residual stress and (b) texture coefficient. Reproduced with permission from ref. [21] ©Elsevier

An interesting observation is that the microstructure has a strong connection with electro-optical properties. Macrostrain increases with tilt angle (figure 13) which is suggestive of presence of tensile residual stress. Again lattice elongation along c-direction is prominent at a higher residual stress. A greater lattice elongation in the [001] direction is favourable for low sheet resistance (figure 14) which might be due to greater degree of delocalization of conduction electrons.

Table II: Transmittance, sheet resistance, figure of merit, sheet carrier density and Hall mobility of ZnO/Ag/ZnO multilayer thin films

Sample	Transmittance (%) at 500 nm	Sheet resistance (Ω/sq)	Figure of merit ($\times 10^{-3}\,\Omega^{-1}$)	Sheet carrier density (cm^{-2})	Hall mobility (cm^{2}V^{-1}s^{-1})
A	65.6	4.56±0.0002	3.30	1.71×10^{15}	9.4
B	72.2	12.77±0.0006	3.04	1.60×10^{15}	9.8
C	60.7	14.0±0.0007	0.48	1.67×10^{15}	9.6
D	77.3	14.71±0.0007	4.94	1.59×10^{15}	9.9
E	65.1	30.0±0.0014	0.46	1.57×10^{15}	10.0
F	72.6	26.0±0.0013	1.32	1.43×10^{15}	10.6
G	81.8	17.0±0.0009	7.87	1.53×10^{15}	10.2

Another way of enhancing conductivity of ZnO is to carry out intense doping with aliovalent elements (B, Al, and Ga). Undoped ZnO is n-type due to native defects but conductivity is not upto the acceptable level of a transparent conductor [4]. Thankfully, ZnO can sustain heavy doping of Al or Ga without substantial structural distortion which leads to dramatic improvement of conductivity of Al-doped ZnO (AZO) and Ga-doped ZnO (GZO) thin films. Recent findings on AZO thin films prepared by magnetron sputtering using AZO sputtering targets are inspiring and as AZO films are potential candidates to replace expensive and toxic ITO [4].

6. Summary and the road ahead:
Nanoscale phenomena are governed primarily by two effects – surface or interface effect and quantum effect. Thin films with specific restriction on thickness (two dimensional), nanowire, nanorods, nanotubes (one dimensional), and nanocrystals/nanoparticles (zero dimensional) are the basic low dimensional structures which exhibit fascinating properties compared with traditional three dimensional structures. Nanosized ZnO and its derivatives are a class of materials which can be easily produced through cost effective route with diverse morphology which in turn control their multi-functional behaviour. The broad prospects of these materials have opened up possibilities of realizing nano-objects and nano devices which are non-toxic, miniaturized and efficient. Although nanotechnology using ZnO derivatives are considered fertile and vibrant domains, even then several issues still remain vague, might be due to the complexity arises at the bottom which provides researchers and

technologists a better avenue to look into the deeper view of reality.

7. Acknowledgements:

8. References:
[1] L. Schmidt-Mende, J. L. MacManus-Driscoll, *ZnO – nanostructures, defects, and devices*, **Materials Today 10 (2007) 40–48**

[2] Z. L. Wang, *Zinc oxide nanostructures: growth, properties and applications*, **J. Phys.: Condens. Mater. 16 (2004) R829–R858**

[3] G. D. Scholes, G. Rumbles, *Excitons in nanoscale systems*, **Nat. Mater. 5 (2006) 683–696**.

[4] B. K. Sarma, P. Rajkumar, B. Sarma, *An improved AZO sputtering target for manufacturing transparent conducting film and the method thereof*, **2018 Indian Patent Appl. No. 201831022820**.

[5] J. D. Plummer, M. Deal. P.B. Griffin, **Silicon VLSI technology: fundamentals, practice and modeling**, Prentice Hall Electronics and VLSI Series, 2000.

[6] Ü. Özgür, Ya. I. Alivov, C. Liu, A. Teke, M. A. Reshchikov, S. Doğan, V. Avrutin, S.-J. Cho, H. Morkoç, *A comprehensive review of ZnO materials and devices*, **J. Appl. Phys. 98 (2005) 041301**.

[7] Z.L. Wang, J. Song, *Piezoelectric nanogenerators based on zinc oxide nanowire arrays*, **Science 312 (2006) 242–247**.

[8] B. Sarma, B. K. Sarma, *Fabrication of Ag/ZnO heterostructure and the role of surface coverage of ZnO microrods by Ag nanoparticles on the photophysical and*

photocatalytic properties of the metal-semiconductor system, **Appl. Surf. Sci. 410 (2017) 557–565**.

[9] S. Reineke, *Complementary LED technologies*, **Nat. Mater. 14 (2015) 459–462.**

[10] G. Lozano S.R.K. Rodriguez, M.A. Verschuuren, J.G. Rivas, *Metallic nanostructures for efficient LED lighting*, **Light: Sci. Appl. 5 (2016) e16080**.

[11] L. Vayssieres, *Growth of arrayed nanorods and nanowires of ZnO from aqueous solutions*, **Adv. Mater. 15 (2003) 464–466**.

[12] B.K. Sarma, A.R. Pal, H. Bailung, J. Chutia, *Role of ion energy on growth and optical dispersion of nanocrystalline TiO_2 films prepared by magnetron sputtering with ion assistance at the substrate*, **Appl. Surf. Sci. 258 (2012) 5659–5665**.

[13] R. Eason, **Pulsed laser deposition of thin films: Application-led growth of functional materials**, Wiley, 2007.

[14] B. Sarma, P. Rajkumar, B.K. Sarma, *Microstructural evolution and optical dispersion of sputtered ZnO thin films at low annealing temperature*, **Mater. Res. Exp. 6 (2019) 016420**.

[15] C.B. Ong, L.Y. Ng, A.W. Mohammad, *A review of ZnO nanoparticles as solar photocatalysts: Synthesis, mechanisms, and applications*, **Renew. Sustain. Energy Rev. 81 (2018) 536–551**.

[16] A. Fujishima, K. Honda, *Electrochemical photolysis of water at a semiconductor electrode*, **Nature 238 (1972) 37–38**.

[17] K. Hashimoto, H. Irie, A. Fujishima, *TiO_2 photocatalysis: a historical overview and future prospects,* **Jpn. J. Appl. Phys.44 (2005) 8269–8285**.

[18] J. Cao, T. Sun, K.T.V. Grattan, *Gold nanorod-based localized surface plasmon resonance biosensors: A review*, **Sens. Actuator. B: Chem. 195 (2014) 332–351**.

[19] H.A. Atwater, A. Polman, *Plasmonic for improved photovoltaic devices*, **Nat. Mater. 9 (2010) 205–213**

[20] X.D. Zhou, X.H. Xiao, J.X. Xu, G.X. Cai, F. Ren, C.Z. Jiang, *Mechanism of the enhancement and quenching of ZnO photoluminescence by ZnO-Ag coupling*, **Electron. Phys. Lett. 93 (2011) 57009–57014**.

[21] B. Sarma, B.K. Sarma, *Role of residual stress and texture of ZnO nanocrystals on electro-optical properties of ZnO/Ag/ZnO multilayer transparent conductors*, **J. Alloys Compd.734 (2018) 210-219**.

Bulletin of Physics Projects

Fabrication of a MOSFET-based low-cost inverter for domestic purposes

Madhubala Baruah, Kishore Dutta[#]

Department of Physics, Handique Girls' Guwahati, Assam, India

[#] Corresponding author's e-mail address: kdkishore77@gmail.com

Abstract

We design a low-cost inverter circuit using transistor and MOSFETs motivated by the growing demand due to frequent power shortages. As an undergraduate laboratory experiment, the circuit constructed from transistors, capacitors, resistors, and n-channel enhancement MOSFETs works in three stages: astable multivibrator, oscillatory circuit, and step-up of the voltage. It produces a 50 Hz AC signal which is then fed into a step- up transformer. We find that the circuit transforms a 12 Volt DC input to a 160 Volt AC output. Higher voltage rating can be achieved by enhancing the stage of oscillation.

1. Introduction:

In today's technological world, the demand in energy consumption, energy saving, explorations of alternative energy sources are growing day by day. Search for alternating energy source now-a-days is an open challenging problem. Apart from this, due to lack of sufficient electric power generation, inverter has become a highly demanding equipment used in every residential and commercial places [1, 2]. An inverter drives the power from DC power banks, like lead acid battery pack. The most common type of inverter we see in everyday life is uninterruptible power supply (UPS) that are used to keep personal computers running in the event of power cuts. Designing a low cost inverter is therefore a highly demanding challenge which can mitigate the needs of power for economically weak people during the time of load shedding. Keeping this in mind, an attempt has been

made in this project to design a low cost inverter circuit which can generate a sufficient amount of AC voltage for domestic purpose. The branded inverters available in the market comprises of ICs, Op-Amps, and 555 timer, making it very expensive. However, without using ICs, a low-cost DC to AC inverter can be designed as done in this project. It comprises only low-cost transistors, n-channel enhancement MOSFETs, and a step-up transformer [3, 4].

2. Experimental Details:

The basic idea behind a working inverter circuit is to convert a DC signal to a constant oscillation and apply these oscillatory signals across the primary of a suitable step-up transformer to obtain the desired AC voltage. The circuit that is designed for this purpose thus works in three successive steps: (a) astable multivibrator (b) MOSFET-based oscillator circuit and (c) Stepped up the voltage using transformer. The circuit designed in this project work

is shown schematically in Fig. 1, showing clearly the various components used in the circuit. It requires (a) a
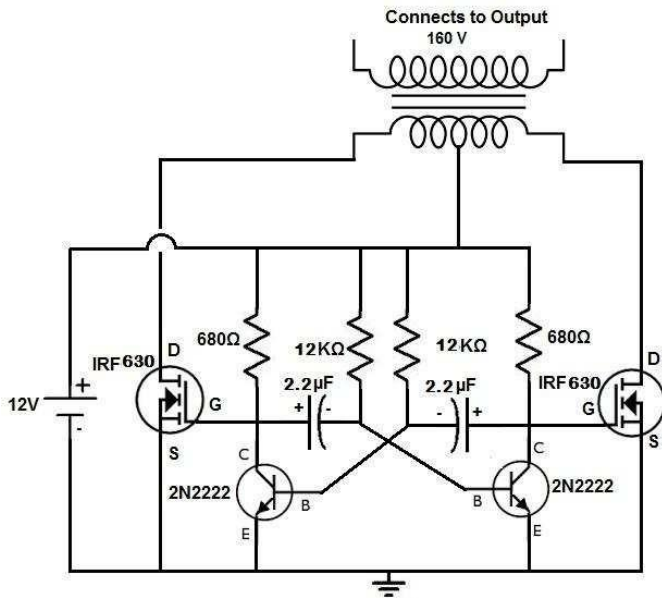
Figure 1: Schematic circuit diagram of the inverter

12V DC Battery (b) a center-tapped 2 Amp step-up transformer (c) two IRF 630 n-MOSFET (d) two 2N2222 transistors (e) two 2.2 μF Capacitors (f) two 680 Ω resistors and (g) two 12 KΩ resistors.

2.1. Working Principle behind the circuit
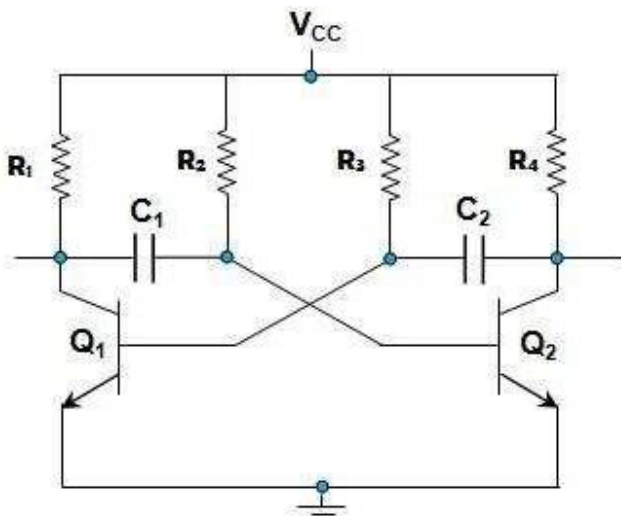
Figure 2: Circuit diagram of astable multivibrator

In the first step of the functioning, there is an astable multivibrator, also known as a free running multivibrator that possesses no stable states. This is constructed using the transistors, capacitors, and resistors, as shown separately in Fig. 2. Its output oscillates continuously between its two unstable states without the aid of external

triggering. The time period of each states are determined by the values of the resistors and capacitors used in the circuit. As shown in Fig. 2, the two transistors are working together as a switch. When one of the transistors is ON, its collector and emitter act as a short circuit while in the OFF mode, they act as an open circuit. In the OFF state, the collector of the transistor possesses a voltage V_t while in the ON state, the collector turns out to have zero voltage (grounded). When the circuit is switched ON, one of the transistors will be conducting more than the other due to imbalance in the circuit or difference in the parameters of the transistor. Finally, depending on the time constant, it will be driven to saturation (ON) and the less conducting transistor will be driven to cutoff (OFF). Lets assume that the transistor Q_1 is in ON state and Q_2 is in OFF state. During this time capacitor C_2 is charging to V_t through resistor R. During this time, Q_2 remains OFF due to the negative voltage from the discharging capacitor C_1 which is charged during the previous cycle. Thus, the OFF time of Q_2 is determined by time constant $T_1 = R_1 C_1$. After this time period, the capacitor C_1 discharges completely and starts charging in reverse direction through R_1. The negative voltage from the capacitor C_2 turns OFF the transistor Q_1 and the capacitor C_1 starts charging from V_t through resistor R and base emitter of transistor Q_2. Thus the transistor Q_2 remains in ON state. As in the previous state, when the capacitor C_2 discharges completely, it starts charging towards opposite direction through R_2. When the voltage across the capacitor C_2 is sufficient to turn ON transistor Q_1, it will turn ON and the capacitor C_1 starts discharging. This process continues and produces rectangular waves at the collector of each transistor.
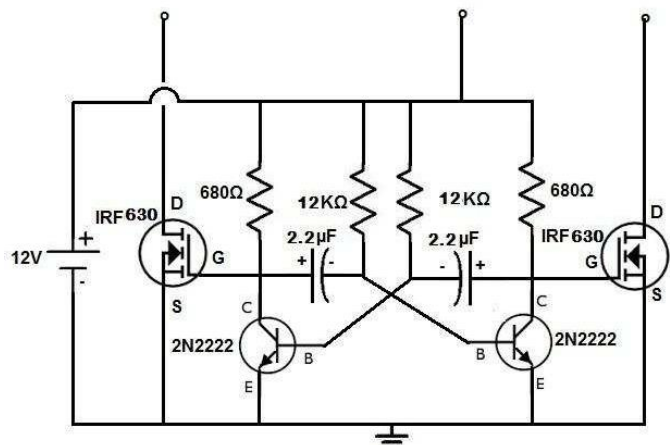
Figure 3: Circuit diagram of MOSFET based oscillatory circuit

In the second step, the signal from the astable multivibrator needs to be fed into a circuit that can generates a constant desired oscillation. We use MOSFET-

based oscillator circuit, as shown in Fig. 3. It comprises two IRF 630 n-MOS. Each n-MOS has three terminals: Gate, Drain, and Source. The Gate terminals of the MOSFETs are connected to a 12 $K\Omega$ resistors through a 2.2 μF capacitor as shown in the diagram. It is also fed by the collector of each transistors used in the astable multivibrator circuit. The Source terminals of each MOSFET are connected to the Emitter of the transistors to enhance the frequency produced by the astable multivibrator. Finally, the oscillatory signal generated by the n- MOS is used as an input to the step-up transformer by connecting the Drain terminals of each MOSFETs to the primary coil of a step-up transformer. The center-tapped step-up transformer has a three terminal input with two extreme terminals connected to the Drains and the center one is connected to the positive terminal of the supply voltage (12 Volt DC battery). In fact, it is also connected to the collector terminals of the transistors. This way the n-MOS based oscillatory circuit is able to generate a high AC voltage having frequency ~50Hz.

3. Results and Discussions:

As shown in Fig. 1, the circuit for the inverter is assembled by connecting the circuits for astable multivibrator, n-MOS oscillator circuit and the step-up transformer as discussed above. With this circuitry, the output terminal of the step-up transformer with its center- tap connected to 12V DC, is connected to a 220 Volt 60 Watt bulb. When the circuit is switched on, the bulb glows and we measure the output AC voltage by using an AC voltmeter and its frequency by a digital multimeter. We find that the frequency of the AC signal is $f \approx$ 50Hz and the output AC voltage is 160 Volt. The frequency of the oscillator circuit can further be enhanced by using a series of MOSFETs in succession. Further, the output AC voltage can be increased by using a step-up transformer with more turn's ratio.

Figure 4: The working circuit configuration in the laboratory

4. Conclusions

The circuit designed here is an initial attempt to develop a low-cost domestic purpose inverter that generates a desired amount of AC voltage for emergency. Although in our experiment we obtain a 50Hz, 160 Volt AC output, the circuit can easily be reconfigured by using more numbers of MOSFETs and a step-up transformer having high turn's ratio so that desired output can be achieved. Since 160 Volt is sufficient to glow a number of 20-30 Watt Compact fluorescent lamp (CFL), it can be used effectively in domestic purpose in emergency.

5. Acknowledgement:

6. References

[1] Louis Nashelsky and Robert Boylestad, *Electronic devices and circuit theory*, Pearson, Eleventh Edition (2015)

[2] Thomas L. Floyd, *Digital Fundamentals*, Prantice Hall, Ninth Edition (2006)

[3] Electronics Magazine, Electronics Weekly, Circulation-40, 918 (2007)

[4] Electronics Today International, 20, No. 4 (1990)

Bulletin of Physics Projects

Journal homepage: http://www.bbcphysics.in/index.php/journal

Solid State Nuclear Track Detector (SSNTD) and its application

Amar Das

Department of Physics, Gauhati University, Jalukbari, Guwahati-781014

email-amarbhdas@gmail.com

Abstract

Alpha particle tracks can be studied by measuring the diameter of alpha particle tracks using solid state nuclear track detector (SSNTD). SSNTD is a track forming material and it can store tracks .For the formation of track, a track forming material should have some characteristics such as low free carrier density, low carrier mobility, high resistivity etc. The sensitivity of different track forming material is different. From the study, it is found that the diameter alpha particle track is in the range of 1-10 micrometer. SSNTD can be used for the study of radon concentration, identification of elements, blood purification and many more. SSNTD are used in most of the branches of the science. So it becomes an important tool for science. In my study the diameter of alpha particle track found to be 7.24 micrometer by using LR-115.

1. Introduction:

The science of solid state nuclear track detector was first introduced by D A Young [2] in 1958 when working at the Atomic Energy Research Establishment (AERE) at Harwell, England. Young observed that when Lithium Fluoride crystal placed 1mm away from Uranium Oxide film were irradiated by thermal neutrons, the surface of the crystal shows number of shallow etch pits after treatment with the chemical reagent ($HF+CH_3COOH$) and saturated iron trifluoride. The number of pits had one to one correspondence with the fission fragments recoiling into the crystals from the uranium foil. Thus a particle detector was born, but its potential was not realized until three more years. Young had recognized the existence of tracks and demonstrated that tracks could be etched and made optically visible and explained the track formation as

a resultant trails of damage left behind by the passage of fission fragments. In 1959, E C H Silk and R S Barnes [3] of AERE Harwell directly observed the damage region produced by fission fragments in thin sheet of mica under transmission electron microscope. The work published by Young was not known to them .The credit for development of particle detector from the observation of tracks due to damage by fission fragments goes to R L Fleischer, P B Price and R M Walker in 1961 [4]. After that, field has grown to such an extent that currently in most of the field of science and technology it finds its application. In this work LR-115 is used for our study.

2. Experimental Details:

Charged particles transferred their energy to matter through Coulomb interaction with the atomic electrons, thus inducing excitation or ionization of the atoms. The

form in which the converted energy appears depends on the detector and its design. The gases detectors for example, are design to directly collect the ionization electrons to form an electric current signal, while in scintillators, the excitation and successive de-excitation contribute to inducing electron transitions which result in the emission of light. Similarly, in photographic emulsion, solid state nuclear track detector (SSNTD), the ionization induces chemical reactions which allow a track image to be formed and so on. [1]. The damage part or trails have greater chemical activity than that of bulk materials. This is due to the disorder structure which contains large free energy. In this method the material with damage trails are immersed in a suitable chemical solution. The reagent reacts with the damage trails more than with the undamaged portion or bulk material. The decomposition of deposited damage parts and precipitated in the solution and visible tracks. The process of enlarging the track dimension by chemical action is called chemical etching. For formation of track chemical etching the rate of etching along the track (V_T) should be greater than rate of etching of the bulk material.

3. Results and Discussions:

In this measurement, four set of observations have been taken and their mean diameters and standard deviations are calculated by the equation 1 and 2 respectively:

$$d_{mean} = \sum f_i d_i / \sum f_i \quad .... (1)$$

$$\sigma_{mean} = \sqrt{[(\sum d_i - d_{mean})^2/(n-1)]} \quad (2)$$

The figure1 shows the alpha LR-115 with alpha tracks.
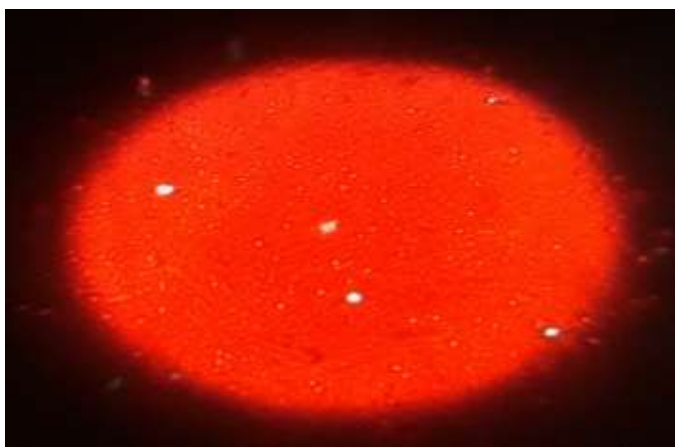
Figure 1: LR-115 with alpha particle tracks

The frequency distribution of the mean diameter for all tracks are plotted in figure 2 for LR-115. The probability density function of a distribution function is given by:

$$P(x) = 1/\sqrt{(2\pi x_{mean})} \exp(-(x_i - x_{mean})^2/2x_{mean}) \quad ....(18)$$

From the estimated values of the mean diameter, the probability density functions are drawn and plotted in figure2.
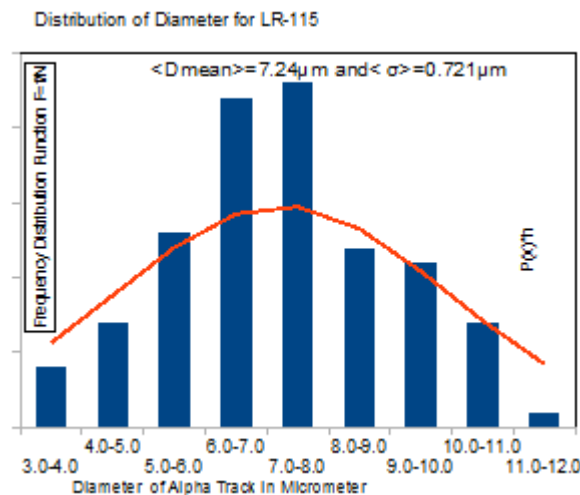
Figure 2: Distribution of Diameter of alpha particle tracks

3. SSNTD and its application:

Since long back, the search for low cost but efficient radiation detection instrumentation is being continued in the Nuclear Physics and Radiation Laboratories. Even though a number of attempts have been made by several workers, finally in 1961, it was R L Fleischer, P B Price and R M Walker could succeed to develop such a low cost but efficient particle detector what is known as Solid State Nuclear Track Detector, or more popularly known as SSNTD. They showed that poor semiconductors and insulators could be used to detect and characterise various charged particles through the technique of optical visualization of their damaged trails in the medium using chemical etching. Immediately after this discovery, the field of SSNTD has undergone a phenomenal growth and has achieved the status of a separate scientific discipline in its own right.

The Solid state nuclear track detector (SSNTD) where it has got well established applications include fission and nuclear physics, space physics, study of meteoritic and lunar samples, cosmic rays, particle accelerators and reactors, metallurgy, geology and archaeology, medicine and biology and many others [5-10].

3.1 SSNTD in geochronology:

Most of the materials contain some traces natural Uranium. Some Uranium atoms have been decaying by spontaneous fission process. Some latent damage trail in the material is created by fission fragment. Density of latent damage trails is proportional to product of age of the material and the Uranium content. Age of the solidification can be known by knowing the uranium content of the material. This is fission track dating. This method is used in dating of geological, archaeological, cosmological samples and also in ocean bottom spread and continental drift. It is also used in distribution of Pu, U, Th, B, Pb, Bi. Plastic track detector is also used in measurement of uranium and thorium.

3.2. SSNTD in seismology:

SSNTD can be used in the **prediction of earthquake**. Many changes taking places in earth crust, small fractures releases radon gas which are trapped within the ground and the changes takes place in that region prior to major physical jolt of an earthquake. Under favourable conditions radon intensity as a function of time should be co-related. It changes with seismic activity in the area. This kind of information can be used to predict the earthquake.

3.3. Cosmological application:

SSNTD can be used in the measurement of cosmic rays fluxes at high altitude and track studies. Apollo and Luna samples gives information concerning their past radiation and thermal histories. The dynamical process on moon-track analysis along with the micro crater studies gives interesting information concerning the composition and fluxes of micrometeoroids in space. In past tracks analysis gives the information about- (i) the erosion and accretion rates on lunar surface, (ii) the original size of meteorites to their loss mass caused by ablation while entering the earth's atmosphere, (iii) the tektites' fall time to the earth and (iv) the existence of fluxes of cosmic rays during different periods of time.

3.4. Application in material science:

Various experiences shows that when the dimension of the artificial structures approach or becomes small that particular characteristic dimensions such as wavelength mean free path, coherence length and molecular sizes it becomes possible to access material in new and different ways, thus giving an new approximation of nuclear tracks

in solid. Such application is possible due to the ability of nuclear tracks to influences the global properties of the materials through structural changes in region. One of the most important examples of such application is in firing magnetic optics iron garnets. Latent tracks as well as etched tracks can be applied for the purpose of changing magnetic materials.

3.5. Biological application of SSNTD:

Use of producing "through holes" by etching latent damage trails has also helped in making filters. The size, shape, position and number can be controlled through experimental details. In **filtering of cancer cells from human blood** and cleaning of air from dust particles SSNTD can be used as filters. SSNTD also been made in the radiobiology of plutonium. One of the importance of such studies due to the extensive involvement of scientists in plutonium production and latent danger of its increased intake by the personal working with it. SSNTD's also been used to find location of plutonium concentration in living matter. The method is very simplest one. The detector is placed in contact under study and a direct autograph is taken of natural alpha decay is obtained, another a rapid mapping is by irradiating the detector tissue assembly by thermo neutron in a reactor. An image resolution of about 10μm or better can be achieved by using SSNTD's. In medical diagnostics it is much important to study the living cells. Conversional flow cytometry uses capillaries with inner between 10μm to 100μm. The economical uses of etched tracks employs one single etched track count, size and measure the electro kinetics mobility of submicrons size particles. The size diameter of red blood cells is about 7.5 μm and its thickness is in between 1-2 μm. The dough nut shaped healthy red blood cells are extremely flexible and easy squeeze through the considerably finer capillaries of human body, the diameter is in between 3-5μm. Many diseases of heart and circulatory system have been traced to an insufficient deformability of red blood cells. The drug influences the characteristics' of red blood cells. It shows that with passage times these cells through single pores can yield important information about rigidity of these cells. It is found that stiffer the cell longer it takes to pass through the pores of nuclear track micro filter. The single pore membrane is the control unit of a measuring cell, which can be divided into lower and upper compartment. The measuring pore has precisely have diameter about 5μm.

Only one human red blood cell at a time can 'squeeze' itself through artificial capillaries. It is important to maintain a constant pressure difference between upper and lower compartments. A number of red blood cells are measured in succession to obtain the passage time spectrum representing various deformability.

3.6. Elements analysis using SSNTD:

SSNTD can be used for measurement and concentration and distribution of a number of elements (uranium, lead, boron, lithium) in a variety of material. The requirement is that some high ionizing reaction products should emanate from samples under study. The incident particles upon hitting the samples form reaction products which produce latent trails in the track detector. The detector is subsequently etched and canned. The spatial resolution of such method is limited primarily by the range of reaction products in etched track detector. The resolution will amount to about 10μm, example in case of uranium in silicate minerals. If isotopes of the element of interest is radioactive and emits alpha particles, it may be possible to carry out elements mapping without any irradiation. SSNTD also found application in bird altimetry and lithography. SSNTD techniques can be used to measure the lead contents and its distribution in teeth and bone and to relate it if possible with age of person. Radioactive isotopes ^{206}Po and ^{210}Po are produced from 206, 207, 208, Po bombardment with ^{3}He ^{4}He. They have half life 8.8 and 138 days respectively. Teeth and bone show increase of lead with increase of age giving clear indication that lead enters blood through food and inhalation of car exhausts and industrial pollutions.

4. Summary and conclusion:

In this work, an attempt has been made to study the response characteristics of alpha particles tracks in LR-115 detector. The track diameters of the alpha particles after passing through the detector are studied. The measured value of the diameter of the alpha particles from the experiment is found to follow approximately a Gaussian distribution for the studied detector. The mean value of diameter of the tracks in LR-115 is found to be 7.24 μm. Diameter of alpha particle track is in the range 1-10 μm hence, the LR-115 detector is better for track counting in radon estimation.

The standard deviation of tracks in LR-115 is also found to be 0.721μm which shows large variation of diameter of alpha tracks. It helps in the estimation of radon concentration. This detector is very much useful for identification of particles from proton to iron in areas where supply of power is not possible.

Reference

[1]. Leo, R. W (1987), Techniques for Nuclear and Particle Physics Experiments A How to Approach.

[2]. Young, D.A., (1958), Etching of radiation damage in lithium fluoride, Nature, **182, 375- 377.**

[3]. Sijk, E.C.H. and Barnes, R.S., (1959), Examination of fission tracks with an electron microscope, Phil.

[4]. Fleischer, R.L., Price, P.B. and Walker, R.M., (1975), Nuclear Tracks in solids: Principles & Applications, University of California Press, Berkeley.

[5]. Fleischer, R.L., Price, P.B., Walker, R.M. and Hub-bard, E.L., (1967b), Criterion for registration in dielectric track detectors, Phys. Rev., 156, 353-355.

[6]. Bhagwat, A.M., (1983), Charged particle track visualisation and evaluation in plastic track detectors and their applications to problems in radiation dosimetry. Ph.D Thesis, Gujarat University.

[7]. Durrani, S.A. and Bull, R. K.. (1985), Solid State Nuclear Track Detectors : Principles, Methods and Applications, Pergamon Press, Oxford.

[8]. Fleischer, R.L., Price, P.B., Walker, R.M. and Hub-bard, E.L., (1967a), Criterion for registration in various solid.

[9]. Fujii, M., Yokota, R. and Atarshi, Y., (1990), Development of polymeric track detectors of high sensitivity, Nucl.Tracks Radiat. Meas, 17,19-21.

[10]. Paretzke, H.G., (1977), On primary damage and secondary electron damage in heavy ion tracks in plastics, Radiat. Effects, 34,3-8.

[11]. Katz, R. and Kobetich, E.J. (1968), Formation of etchable tracks in dietectrics, Phys. Rev., 170, 391-396.

[12]. Solid state nuclear track detection (ssntd) useful scientific tool for basic and applied research reviewed article by Hameed Ahmed Khan and Naeem Ahmed Khan.

Bulletin of Physics Projects

A Brief Study of Periodic Doubling in Dripping Water

Abhisek Sengupta, Arnab Mukharjee, Ivapriti Saharia, Akhil Ch Das[#]

Department of Physics, B. Borooah College, Guwahati - 781007

[#] **Corresponding author's e-mail address: akhilchdas@gmail.com**

Abstract

With the emergence of nanotechnology, two, one and zero- dimensional structures are of great interest as they demonstrate size dependent material properties different from their bulk counterpart. To be precise enough, properties are shape dependent as well. Nanostructured ZnO is a low cost and environmentally acceptable semiconductor with high photosensitivity, photocatalytic activity and piezoelectric properties. This topical review presents current scenario of ZnO and its derivatives – metal-semiconductor heterostructure, piezoelectric nanogenerators, and transparent conductors where well defined morphology, microstructure, and interfacial properties are crucial for specific applications.

1. Introduction:

Dripping of water drops from tap or faucet is a familiar phenomenon. It is a simple example of chaotic dynamical system. O.E.Rössler [1] gave a model of the dynamics of dripping water drops from a faucet and suggested that it could exhibit chaotic behaviour. After that another researcher Robert Stetson Shaw [2] also started to study the same phenomenon using computer simulations. An experimental investigation was carried out by P. Martien [3] in 1985 regarding the behaviour of dripping water drops from a faucet for different flow rates. His investigation was followed by several experimental studies by different researchers which resulted in improvements of theoretical models and apparatus used for the study of the water dripping phenomenon. During these studies along with chaotic behaviour other interesting factors related to the dripping process such as strange (chaotic) attractors, periodic doubling, quasi-periodicity, boundary crisis and Hopf bifurcation etc. were observed.

2. Theory:

Dripping of water drops from a faucet or a tube of small bore is a complex phenomenon. In the study of the phenomenon of the dripping water drops, their formation, shape, detachment and periodicity of the falling drops are important. In broad sense the study of the phenomenon can be divided into two categories: (1) formation and oscillation of a drop at the nozzle of the faucet and (2) periodicity of the falling drops.

2.1 Formation and oscillation of a drop at the nozzle of the faucet:

Formation of the drop at the nozzle of the faucet is modeled as a damped harmonic oscillator. The mass-spring model of the forming drop from the residual mass at the nozzle of the faucet given by Shaw is the simplest one. During its formation the water drop is considered as 'mass' driven by the flow of water into it which increases the mass of the drop linearly with time. When the position of the centre of mass of the drop formed at the nozzle of the faucet reaches a critical value (measured from the level of the nozzle) the mass of the drop is reduced by pinching off of a large part of the drop. Immediately after dropping down of the large part of the drop remaining smaller part begins to grow again. The centre of mass of the growing drop begins to oscillate like a damped harmonic oscillator. Basically, three forces are acting on the oscillating drop -

(i)   Downward force due to gravity: mg

(ii)   Upward restoring force due to surface tension: -ky

(iii)   Upward drag force due to viscosity: -bv

where,

m = mass of the drop at a particular instant of time t,

g = acceleration due to gravity,

y = position of the centre of mass of the drop as measured from the level of the nozzle at the same instant t,

k = time dependent (mass of the drop increases linearly with time) spring constant (contributed by surface tension of water),

b = drag coefficient (contributed by viscosity of water)

$v = \dfrac{dy}{dt}$ velocity of the oscillating drop at instant of time t

Thus the equations of motion of the drop can be written as-

$$\frac{d(mv)}{dt} = mg - ky - bv \qquad (1)$$

$$\frac{dm}{dt} = flow.rate \qquad (2)$$

Here, equation (1) describes the oscillatory motion of the growing drop, and equation (2) gives its rate of growth.

2.2 Periodicity of the falling drops:

Another important aspect of the dripping faucet is the dependency of periodicity of the falling drops on the flow rate of the water from the tube to the nozzle. With increase in flow rate the periodicity of pinching off and hence falling of drops from the nozzle transforms from periodic (predictable) to chaotic (unpredictable).

In our study we focus our attention in exploring the transition from periodic (predictable) to chaotic (unpredictable) nature of the dripping drops as the flow rate is increased. In chaotic regime the falling drops show a strange nature called periodic doubling. In periodic doubling process, the period of some falling drops become double of that of the previous drops. We aimed to explore this periodic doubling. The formation and oscillation of the drops during detachment from the nozzle is a complicated process which requires high level research and is beyond our scope.

3. Experimental Arrangement:

The experimental arrangement for the study of periodicity of the dripping drops from a faucet consists of two mechanisms:

1) A small bore rubber tube of sufficient length with a regulator and a nozzle fitted to one end to produce water drops at different rates. The other end of the tube is connected to a water reservoir. In our study we use an IV drip set (intervanous drip set used to infuse drugs, saline etc to patients) in which the drip rate can be controlled conveniently. A plastic bottle is used as reservoir for water.

2) A timing mechanism to record the period of falling of the water drops. In our study we have used an IR sensing system along with a 555 timer IC.

The infrared sensing system consists of two parts:-

(i) an IR LED to produce infrared rays and a receiver photo diode capable of detecting the infrared rays produced by the IR LED.

ii) a 555 timer to trigger the signals received by the IR LED. The output of the timer is recorded in an Oscilloscope, preferably a Digital Storage Oscilloscope (DSO).

3.1 Working of the Circuit:

In the circuit shown in figure-1, the transistor Q_1 (BC 547) is a NPN transistor which conducts when it is forward biased by applying a small positive voltage to its base. Similarly, the transistor Q_2 (BC 557) is a PNP transistor which conducts when it is forward biased by applying a small negative voltage to its base or the base is grounded.

When the circuit is switched on the IR LED starts emitting infrared rays. If the position of the photodiode (in general which is operated in reverse biased condition) is adjusted to receive these rays, it will be activated and a current will flow through it which will create a potential difference

across the resistor R_2. This potential difference across R_2 will forward bias the transistor Q_1, which as a result begins to conduct. This brings the base of the transistor Q_2 almost to ground potential due to which it also begins to conduct. As a result, the 555 timer (through pin number 8) gets connected to the power supply and starts working giving some signal of fixed frequency determined by the resistors R_1, R_2, and capacitor C_1. As the 555 timer is operated in astable mode hence the frequency of the output signal is given by

$$f = \frac{1.44}{(R_5 + 2R_6)C_1} \qquad (3)$$

When a falling water drop momentarily obstructs the infrared rays coming from the IR LED the photodiode will temporarily become non-conducting which will make the transistors Q_1 and Q_2 non-conducting and the 555 timer will be cut off from the supply source during that short time interval and there will be no signal at its output. Thus if the output of the 555 timer is fed to an Oscilloscope and water drops from the nozzle of a water tube having a flow regulator mechanism, connected to a reservoir are allowed to drip down through the space between the IR LED and photodiode, the periodicity of the dripping drops can be studied from the wave form displayed by the Oscilloscope.
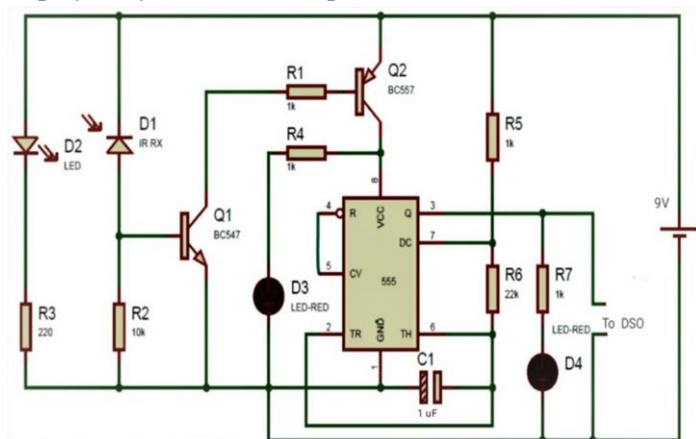
Figure 1: Circuit diagram to study of periodicity of the dripping drops from a faucet

The IV drip set (intervanous drip set used to infuse drugs, saline etc to patients) is filled with distilled water and connected to a water reservoir. The end part (about 1 metre) of the IV drip set along with the nozzle is kept horizontally fixed on a table. Regulator in the drip set is adjusted for slower flow velocity. Then flow velocity, drop

rate, average mass and average radius of the drops for a particular flow rate are determined. Keeping the flow rate constant, dripping drops are allowed to pass through the space between the IR LED and photodiode and output of the timer is fed to an oscilloscope. The wave form displayed in the oscilloscope is videographed using a mobile phone for a certain time interval. Transfering the video to a computer, time interval between consecutive falling drops are determined by observing the video frame by frame.

4. Result and Discussion:

4.1 Determination of frequency of the timer:

$R_5 = 1k\Omega$, $R_6 = 22k\Omega$, $C = 1\mu F$

$$f = \frac{1.44}{(1k\Omega + 2X22k\Omega)1\mu F} = 32\,\text{sec}^{-1}$$

Time period, T = 0.03125 sec

Pulse width = T/2 = 0.015625 sec

4.2 Determination of mass and radius of a drop:

(Flow velocity 3.421cm.sec^{-1})
1. Mass of the empty beaker = 48.064 gm
2. Mass of the beaker with 30 drops = 48.764 gm
3. Mass of 30 drops = (48.764 - 48.064) gm = 0.700 gm
4. Mass of 1 drop, $m_1 = \dfrac{0.700\,gm}{30} = 0.023\,gm$
5. Density of water = 1 gmcm^{-3}
6. Volume of the drop

$$V_1 = \frac{mass}{density} = \frac{0.0023\,gm}{1gmcm^{-3}} = 0.0023cm^3$$

7. Radius of the drop

$$r_1 = \left(\frac{3V_1}{4\pi}\right)^{1/3} = \left(\frac{3X0.0023}{4X3.14}\right)^{1/3} = 0.081cm = 0.81mm$$

4.3 Determination of nozzle & tube diameter :
1. Nozzle diameter = 0.444 cm = 4.44 mm
2. Tube diameter = 0.460 cm = 4.60 mm

4.4 Determination of flow velocity (slow flow rate):
1. Length of the tube, L= 45.5cm
2. Time taken to cover L length :
   t_1 = 8.16 sec, t_2 =7.41 sec, t_3 =7.31 sec, t_4 = 7.38 sec, t_5 = 7.45 sec

3. Average time,

$$t = \frac{8.16 + 7.41 + 7.31 + 7.38 + 7.45}{5} = 7.54\,\text{sec}$$

Average velocity, $v = \dfrac{45.5cm}{7.54\,\text{sec}} = 6.03 cm.\text{sec}^{-1}$

4.5 Determination of time interval between successive drops:

Flow velocity = 6.03 cm.sec^{-1}

Table I

Time interval between successive drops

Serial no. of drop	Time interval w.r.t. just previous drop (sec)	T_n (sec)	T_{n+1} (sec)	Time of fall t (time counting started from n^{th} drop) (sec)
n	0.25	0.25	0.25	0.00
n+1	0.25	0.25	0.25	0.25
n+2	0.25	0.25	0.25	0.50
n+3	0.25	0.25	0.25	0.75
n+4	0.25	0.25	0.25	1.00
n+5	0.25	0.25	0.25	1.25
n+6	0.25	0.25	0.25	1.50
n+7	0.25	0.25	0.25	1.75
n+8	0.25	0.25	0.25	2.00
n+9	0.25	0.25	0.25	2.25
n+10	0.25	0.25	0.25	2.50
n+11	0.25	0.25	0.25	2.75
n+12	0.25	0.25	0.25	3.00
n+13	0.25	0.25	0.25	3.25
n+14	0.25	0.25	0.25	3.50
n+15	0.25	0.25	0.25	3.75
n+16	0.25	0.25	0.25	4.00
n+17	0.25	0.25	0.25	4.25
n+18	0.25	0.25	0.25	4.50
n+19	0.25	0.25	0.25	4.75
n+20	0.25	0.25	0.25	5.00

4.6 Determination of flow velocity (medium flow rate):

1. Length of the tube: L = 45.5 cm
2. Time taken to cover L length:

t_1 = 5.32 sec, t_2 = 5.09 sec, t_3= 5.11 sec, t_4 = 5.20 sec, t_5 = 5.37 sec

3. Average time:

$$t = \frac{5.32 + 5.09 + 5.11 + 5.20 + 5.37}{5} = 5.21\,\text{sec}$$

4. Average velocity, $v = \dfrac{45.5cm}{5.21\,\text{sec}} = 8.73 cm.\text{sec}^{-1}$

4.7 Determination of time interval between successive drops:

(Flow velocity = 8.73 cm.sec^{-1})

Table II

Time interval between successive drops

Serial number of drop	Time interval w.r.t. just previous drop (sec)	T_n (sec)	T_{n+1} (sec)	Time of fall t (time counting started from n^{th} drop) (sec)
n	0.1875	0.1875	0.1875	0.0000
n+1	0.1875	0.1875	0.1563	0.1875
n+2	0.1563	0.1563	0.1563	0.3438
n+3	0.1563	0.1563	0.1875	0.5001
n+4	0.1875	0.1875	0.1563	0.6876
n+5	0.1563	0.1563	0.1875	0.8439
n+6	0.1875	0.1875	0.1875	1.0314
n+7	0.1875	0.1875	0.1563	1.2189
n+8	0.1563	0.1563	0.1563	1.3752
n+9	0.1563	0.1563	0.1875	1.5315
n+10	0.1875	0.1875	0.1875	1.7190
n+11	0.1875	0.1875	0.1563	1.9065
n+12	0.1563	0.1563	0.1563	2.0628
n+13	0.1563	0.1563	0.1875	2.2191
n+14	0.1875	0.1875	0.1875	2.4066
n+15	0.1875	0.1875	0.1875	2.5941
n+16	0.1875	0.1875	0.1563	2.7816
n+17	0.1563	0.1563	0.1563	2.9379
n+18	0.1563	0.1563	0.1875	3.0942
n+19	0.1875	0.1875	0.1875	3.2817
n+20	0.1875	0.1875	0.1563	3.4692

4.8 Determination of flow velocity (fast flow rate):

1. Length of the tube, L = 45.5 cm
2. Time taken to cover L length:

t_1=5.50sec, t_2=4.84sec, t_3=4.78sec, t_4=4.63sec, t_5=3.94sec, t_6=4.31sec

3. Average time

$$t = \frac{5.50 + 4.84 + 4.78 + 4.63 + 3.94 + 4.31}{6} = 4.67\,\text{sec}$$

Average velocity, $v = \dfrac{45.5cm}{4.67\,\text{sec}} = 9.743 cm.\text{sec}^{-1}$

4.9 Determination of time interval between successive drops:

Flow velocity = 9.743 cm.sec^{-1}

Table III

Time interval between successive drops

Serial number of drop	Time interval w.r.t. just previous drop (sec)	T_n (sec)	T_{n+1} (sec)	Time of fall t (time counting started from n^{th} drop) (sec)
n	0.125	0.125	0.0938	0.0000
n+1	0.0938	0.0938	0.0938	0.0938
n+2	0.0938	0.0938	0.0938	0.1876
n+3	0.0938	0.0938	0.0938	0.2814
n+4	0.0938	0.0938	0.0938	0.3752
n+5	0.0938	0.0938	0.125	0.469
n+6	0.125	0.125	0.0938	0.594
n+7	0.0938	0.0938	0.125	0.6878
n+8	0.125	0.125	0.0625	0.8128
n+9	0.0625	0.0625	0.125	0.8753
n+10	0.125	0.125	0.0938	1.0003
n+11	0.0938	0.0938	0.0938	1.0941
n+12	0.0938	0.0938	0.0938	1.1879
n+13	0.0938	0.0938	0.0938	1.2817
n+14	0.0938	0.0938	0.0938	1.3755
n+15	0.0938	0.0938	0.0313	1.4693
n+16	0.0313	0.0313	0.0625	1.5006
n+17	0.0625	0.0625	0.125	1.5631
n+18	0.125	0.125	0.0938	1.6881
n+19	0.0938	0.0938	0.125	1.7819
n+20	0.125	0.125	0.0938	1.9069

4.10 Determination of flow velocity (faster flow rate):

1. Length of the tube: L=45.5cm

2. Time taken to cover L length:
   t_1 = 5.50 sec, t_2 = 4.56 sec, t_3 = 3.25 sec, t_4 = 3.72 sec, t_5 = 4.55 sec, t_6= 3.85sec

3. Average time

$$t = \frac{4.56 + 3.25 + 3.72 + 4.55 + 3.85}{5} = 3.98\,\text{sec}$$

4. Average velocity, $v = \dfrac{45.5cm}{3.98\,\text{sec}} = 11.43 cm.\text{sec}^{-1}$

4.11 Determination of time interval between successive drops:

Flow velocity = 11.43 cm.sec^{-1}

Table IV

Time interval between successive drops

Serial number of drop	Time interval w.r.t. just previous drop (sec)	T_n (sec)	T_{n+1} (sec)	Time of fall t (time counting started from n^{th} drop) (sec)
n	0.0625	0.0625	0.0313	0
n+1	0.0313	0.0313	0.2188	0.0313
n+2	0.2188	0.2188	0.0938	0.2501
n+3	0.0938	0.0938	0.0938	0.3439
n+4	0.0938	0.0938	0.0938	0.4377
n+5	0.0938	0.0938	0.0313	0.5315
n+6	0.0313	0.0313	0.0625	0.5628
n+7	0.0625	0.0625	0.125	0.6253
n+8	0.125	0.125	0.0938	0.7503
n+9	0.0938	0.0938	0.0313	0.8441
n+10	0.0313	0.0313	0.0625	0.8754
n+11	0.0625	0.0625	0.0313	0.9739
n+12	0.0313	0.0313	0.0938	1.0052
n+13	0.0938	0.0938	0.1875	1.099
n+14	0.1875	0.1875	0.0625	1.2865
n+15	0.0625	0.0625	0.0938	1.349
n+16	0.0938	0.0938	0.0938	1.4428
n+17	0.0938	0.0938	0.125	1.5366
n+18	0.125	0.125	0.0625	1.6616
n+19	0.0625	0.0625	0.1563	1.7241
n+20	0.1563	0.1563	0.0938	1.8804

5. Discussion:

5.1 Return map:
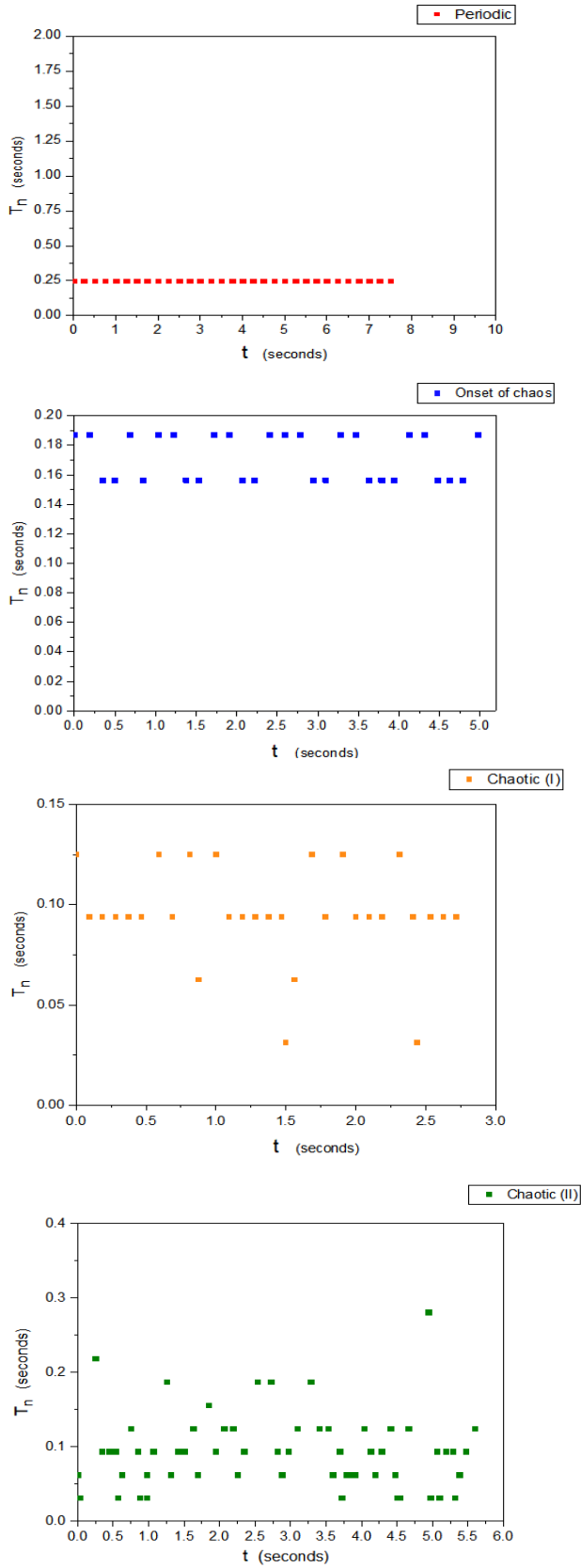
Figure 2: Return map for four different flow velocity and drop radius
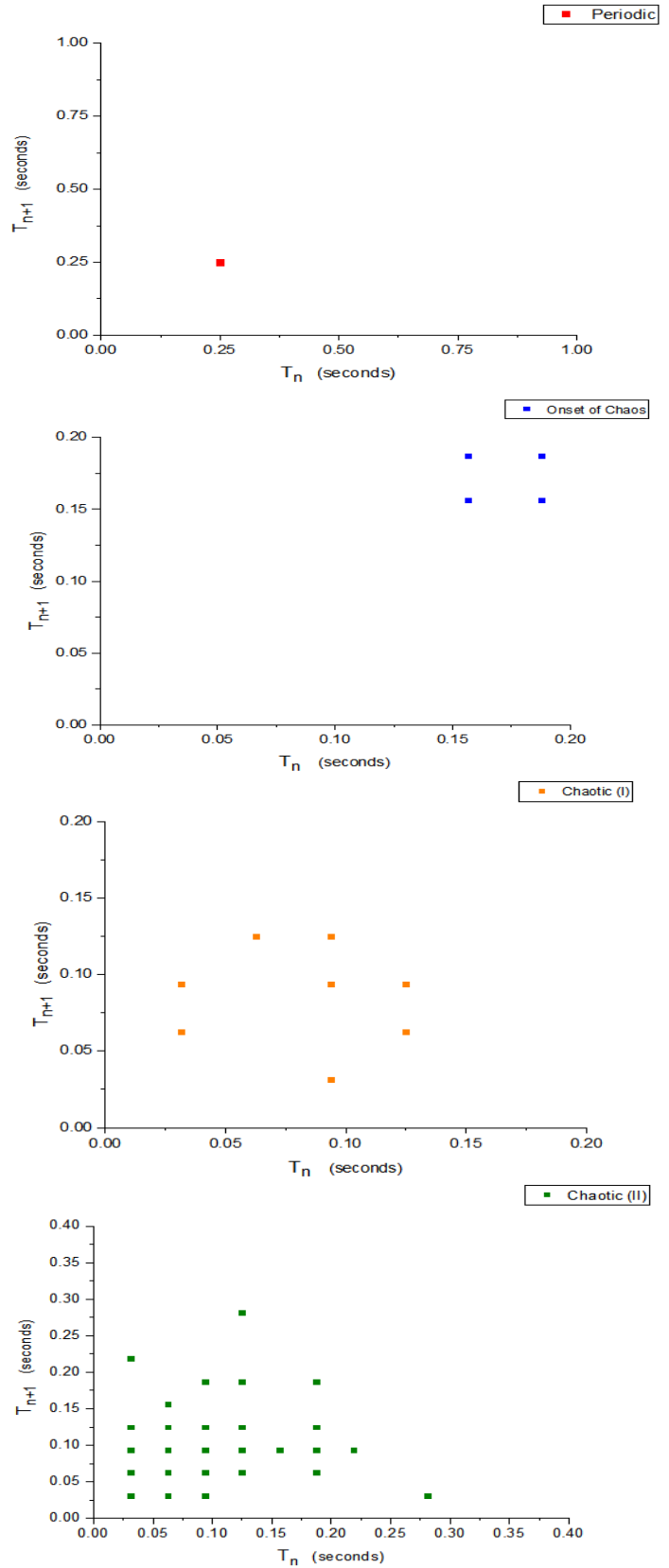
Figure 3: Phase diagram for each flow velocity

A graph plotted between T_n (time interval between two consecutive drops i.e. $(n-1)^{th}$ and n^{th} drop) versus T_{n+1} (time interval between n^{th} and $(n+1)^{th}$ drop) is called a return map. Return maps for four different flow velocity and drop radius are plotted using the above data.

5.2 Phase diagram:

A graph plotted between time of dripping (starting time counting from the dripping of a particular drop) and time intervals which shows how the periods of dripping water drops are changing is called phase diagram. For each flow velocity a phase diagram is drawn from the above data.

5.3 Bifurcation Diagram:

A graph plotted between different flow rate V and T_n (time interval between two consecutive drops i.e. $(n-1)^{th}$ and n^{th} drops) which shows how the behaviour of dripping drops is changing from predicable to unpredictable giving rise to periodic doubling etc. is called a Bifurcation diagram. Bifurcation diagram is drawn taking different flow velocity and corresponding T_n from the above data.

5.4 Histogram:

Histograms are drawn counting the number of same time interval occurred during a certain number of observations for a given flow velocity.

6. Discussion:

Return map-1 for flow velocity 6.03 cm.sec^{-1} and constant dripping rate 4 drops per second has only one point. The phase diagram for this regime is a straight line and the histogram has a single column. From the recorded video, the obstruction duration for all falling drops is found to be 0.015625 sec. All these indicate periodic regime of the dripping drops with single period of interval 0.25 sec.

Return map-2 for flow velocity 8.73 cm.sec^{-1} has four points; two of them are on the line $T_n = T_{n+1}$ and one above and one below the straight line for $T_n = T_{n+1}$ representing periods 0.1875 sec and 0.1563 sec corresponding to approximate dripping rate 5 drops per second and 6 drops per second respectively. The phase diagram shows almost regular changes from one periodicity to another periodicity. The histogram shows equal number of drops dripping from the nozzle in a certain time interval for both the periods. From the recorded video obstruction duration is found to be 0.015625 sec. Two periods for this flow velocity clearly indicates the onset of chaotic dripping and bifurcation of period.
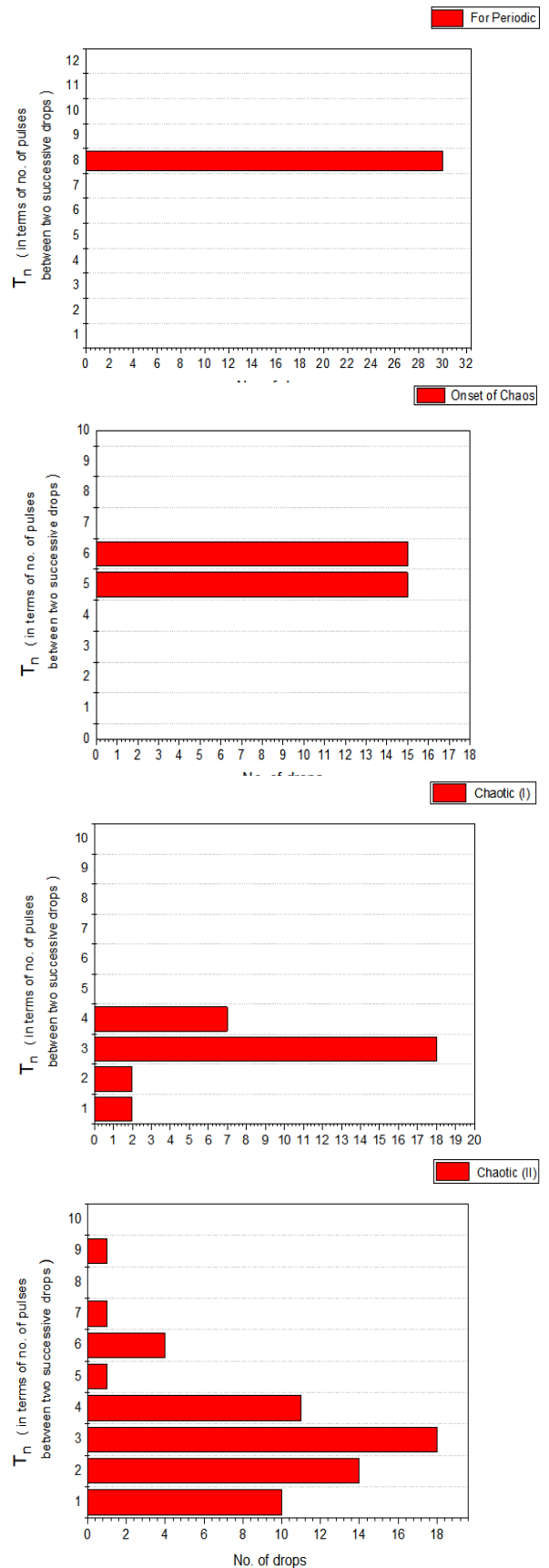
Figure 4: Number of occurrence for different flow velocity

For flow velocity of 9.74cm.sec^{-1} there are four dripping rates 32, 16, 11(10.67) and 8 drops per second with average dripping rate of 17 (16.67) drops per second. The return map-3 for this flow velocity is scattered one. There are seven points, four of them are above and three are below the straight line for $T_n = T_{n+1}$. These points indicate more than one period of different intervals. The presence of these points in the return map-3 clearly indicates period-1, period-2, period-3 and period-4 dripping of water drops. The time interval 0.0625 sec of period-2 dripping is double of the time interval 0.0313 sec that of period-1. Similarly, time interval 0.125 sec of period-4 dripping is double of the time interval 0.0625 sec that of period-2. This clearly indicates the periodic doubling in the chaotic regime. The phase diagram shows irregular changes from one periodicity to another periodicity. The histogram shows drastic decrease of drop number for higher as well as lower drop rates comparison to drop rate of 11 drops per second. From the recorded video two different obstruction durations are found to be present for dripping drop rates. In some cases, it is 0.015625 sec and in some other cases it is 0.0234375 sec. This difference may be due to variable drop size.

For flow velocity of 11.45 cm.sec^{-1} there are eight dripping rates 32, 16, 11, 8, 6, 5, 4, and 3 drops per second with average dripping rate of 11 drops per second. The return map-4 for this flow velocity is also scattered one. There are several points above and below the straight line for $T_n = T_{n+1}$. These points indicate more than one period of different intervals. In the return diagram-4, eight different periods are present from period-1 to period-9 excluding the period-8. The time interval 0.0625 sec of period-2 dripping is double of the time interval 0.0313 sec that of period-1. Similarly, time interval 0.125 sec of period-4 dripping is double of the time interval 0.0625 sec that of period-2.

Again time interval 0.1875 sec of period-6 is double that of the time interval 0.0938 sec of period-3. This clearly indicates more and more periodic doubling in the chaotic regime when the flow velocity is increased. The phase diagram shows irregular changes from one period to another period. In this case also the histogram shows drastic decrease of drop number for higher as well as lower drop rates comparison to drop rate of 11 drops per second. From the recorded video two different obstruction durations are found to be present for dripping drop rates. In some cases, it is 0.015625 sec and in some other cases it is 0.0234375 sec. This difference may be attributed to variable drop size and secondary drops.

From the bifurcation diagram it is seen that as flow velocity increases bifurcation of period increases. For flow velocity 6.03 cm.sec^{-1} with dripping rate 4 drops per second there is only one constant period of 0.25 sec. For flow velocity 8.73 cm.sec^{-1} with dripping rate 6 and 5 drops per second two different periods appears which are 0.1875 sec and 0.1563 sec. For flow velocity 9.47cm.sec^{-1} with dripping rate 32, 16, 11 and 8 drops per second four different periods appear which are 0.0313 sec, 0.0625 sec, 0.0938 sec and 0.1250 sec along with two cases of periodic doubling. When the flow velocity becomes 11.43cmsec^{-1} with dripping rate 32, 16, 11, 8, 6, 5, 4 and 3 drops per second there appears eight different periods 0.0313 sec, 0.0625 sec, 0.0938 sec, 0.1250 sec, 0.1563 sec, 0.1875 sec, 0.2188 sec and 0.2813 sec along with three cases of periodic doubling. It is clear from above discussion that as the flow velocity is increased, dripping of water drops from the nozzle of the tube changes from predictable (single period) to unpredictable (multiple periods) or chaotic one. After the onset of chaotic behaviour the number of periods increases in the sequence of 2, 4 and 8 different periods as the number of dripping drops increases due to increase in flow velocity indicating more and more bifurcation of periods and more and more periodic doubling. For dripping rate of 32 drops per second, the dripping is almost continuous.

6. Conclusions:

Our investigation clearly reveals the existence of periodic doubling in dripping water from a tap or faucet. As mentioned in the introduction, the phenomenon of dripping water from a tap is a complicated one. It depends not only on flow velocity but on several factors like faucet diameter, wall thickness, geometry (cut angle), temperature etc. In case of dripping water, there is enough scope for study, basically about the formation mechanism and standardization of the formation theory by experimental confirmations. Presently different investigations are going on all over the world in this particular area.

Apart from basic study of a chaotic system this method can be used for determination of surface tension and its variation with the increase in mass of the growing drop if the factors involved in equation (1) are known.

From the data of time period for different flow velocity, it is observed that most of the time periods are integral

multiple of a particular period which needs further intensive study.

More interestingly chaos has been already studied and discovered in a wide range of natural phenomena such as weather, population cycles of animals, the structure of coastlines and trees and leaves, biological systems such as rates of heartbeat, and also acoustical systems. Music composers are even trying to use chaotic behaviour, specially the idea of multiple periods in technically generated music using various computer software.

The chaotic behaviour of different natural phenomena is an inherent property and the *near* repetition and *near* periodic regularity produced by a system like dripping water drops in the chaotic regime may result in musically interesting output since they are self-produced natural patterns with some externally controllable factors.

Undoubtedly chaotic behaviour needs some intensive study to explore its potentialities and utilizations.

7. Acknowledgements:

8. References:

[1] O.E.Rössler, Synergetics, A workshop, H. Haken (Ed.), Springer Berlin, 1977, p.174

[2] R. Shaw, The dripping faucet as a model chaotic system, Aerial Press, Santa Cruz, USA,1984

[3] P. Martien, S.C. Pope, P.L. Scott, R.S. Shaw, Phys Lett. A 110 (1985) 399.

Bulletin of Physics Projects

Journal homepage: http://www.bbcphysics.in/index.php/journal

Optical method for measuring optical rotation angle and refractive index of chiral solution:

Kaustav Jit Bora, Dhrubajyoti Goswami, Vasudev Upadhyay, Dipsikha Kalita [#]

Department of Physics, B Borooah College, Guwahati, Assam.

[#] dkalita93@gmail.com

Abstract

In this paper, the angle of rotation of optically active sucrose and fructose solutions of different concentrations has been determined by using half-shade polarimeter. From experimental analysis we have observed that the angle of rotation of polarized light depends linearly on concentrations of sucrose, fructose and natural grape solutions. We have also studied the variation of optical rotation with respect to wavelength using different color filters in front of white light and thus we have analysed the variation of optical rotation of sucrose and fructose (artificial & natural) solutions as a function of wavelength. Moreover, the angle of minimum deviation (obtained from spectrometer analysis) for a solution of a particular concentration gives us the refractive index of the solution at that concentration. In this analysis, the refractive index measurements were carried out for the same solutions employed for study of angle of rotation using the conventional minimum deviation method of an equilateral hollow glass prism. Thus from the analysis of refractive index of solutions of different concentrations, it is observed that the values of refractive indices increase with increasing concentrations.

1. Introduction

Polarization is a property of waves that describe the orientation of their oscillations. A light wave that is vibrating in more than one plane is referred to as unpolarized light or ordinary ray light. It is possible to transform unpolarized light into polarized light by using polarizing filters. The light having wave motion in only one plane is known as plane polarized light. The process of transforming unpolarized light into polarized light is known as polarization. [1,2].

Polarimetry is an optical method used to measure the concentration and purity of a substance in a solution based on angle of rotation of the plane polarized light. A substance is said to be optically active if it rotates the plane polarized light, either left or right. Optical activity of a substance depends on its chirality. The direction of polarization in a plane-polarized light beam gradually rotates on its passage through such solutions. The angle of rotation is proportional to the distance travelled in the liquid, and it is approximately proportional to the sugar concentration. The rotatory power to a considerable degree

is dependent on the wavelength of the light, a phenomenon called rotatory dispersion [4].

The specific rotation of optically active solutions is defined as the angle through which the plane of polarization of a ray of a monochromatic light would be rotated by a column of solution 100 mm in length, l , containing 1 g of substance per cm^3 at 20 ˚C. λ represents the wavelength of the light used and T represents the temperature of the solution during the experiment. It is generally expressed as

$$[\alpha]_\lambda^T = \frac{\alpha}{lc} \qquad (1)$$

Where α **is** the angle of optical rotation, l is the path length (length of the tube) and c is the concentration of the liquid. It is measured in degrees.m^{2}kg^{-1}. Equation (1) is known as the Biot's law. But l is measured in dm and is equal to unity since the tube is 10 cm long. Then the equation (1) becomes:

$$[\alpha]_\lambda^T = \frac{\alpha}{c} \qquad (2)$$

The refractive index (μ) of a prism is measured by Snell's formula given as

$$\mu = \frac{sin\left(\frac{A+\delta_m}{2}\right)}{sin\left(\frac{A}{2}\right)} \qquad (3)$$

Changing the concentration of the solution would also give different values of the refractive index. Now for a given solution of unknown concentration, the refractive index can be determined. Also from the values of the other refractive indices, the concentration of the unknown solution can then be determined. All this should be done at a constant temperature, preferably at room temperature.

2. Materials and Methods:

Sucrose and fructose solutions of different concentrations (2%, 4%, 6%, 8% and so on upto 14%) were prepared at room temperature by dissolving known weight of sugar in fixed volume of distilled water. At first a stock solution of concentration 14% was prepared by mixing 7g of artificial crystalline sucrose with 50mL of water in a volumetric flask for analysis of optical rotation using Sodium-D light. Then the concentration of the source solution is lowered to 12%, 10%, and so on till 2% by adding an amount of water calculated using the formula-

Amount of water to be added,

$$x = \frac{C_1 - C_2}{C_2} \text{ x Volume of stock solution}$$

C_1 = Initial Concentration
C_2 = Final Concentration

Figure 1: Preparation of raw grapes juice sample.

Figure 2: Experimental set up for measurement of angle of rotation for different solutions.

To prepare the grape juice, 250gm of Grapes has been cleaned by water and then dried using blotting paper so that no water molecule stays on the surface of the grapes. The grapes were then grinded on a morter-pastle to prepare the juice and allowed to pass it through a funnel (Figure 1). 5mL of prepared grapes juice is mixed with 95mL of water to prepare 5% concentration of grape juice which is then taken in polarimeter tube to measure the optical rotation. The analysis has been repeated for grape solutions of concentrations from 4% to 1% by adding an amount of water calculated using the same formula as used for sucrose solutions.

To study the variations of optical rotation with concentration for different wavelengths of light, the solutions of sucrose and fructose of different concentrations (2%, 4%, 6%, 8% and so on upto 14%) were prepared following the above procedure. For

obtaining different wavelengths we have used different colour filters in front of the white light source (Figure 2).

Figure 3: (a) Hollow glass prism (b) Experimental set up for analysis of refractive index of different concentrated solutions.

A clean and dry hollow glass prism was filled with the prepared solution and for every sample, angle of minimum deviation δ_m was measured using spectrometer adjusted by Schuster's method (Figure 3). For the measured values of δ_m and angle of prism A = 60^0, the refractive index (μ) of sample was computed using the Snell's formula stated earlier. The values were recorded separately.

3. Results and Discussions

3.1 Study of variation of optical rotation with concentration: [Using Sodium-D Light]

To study the variations of optical rotation with concentration for different wavelengths of light, the solutions of sucrose and fructose of different concentrations (2%, 4%, 6%, 8% and so on upto 14%) were prepared following the above procedure. For obtaining different wavelengths we have used different colour filters in front of the white light source.

The graph of angle of rotation against concentration is a straight line for sucrose, fructose and grape solution. Given a solution with an unknown concentration, its optical angle of rotation can be determined experimentally and the graph is either interpolated or extrapolated to determine its concentration. The gradients $\left[\frac{d\alpha}{dc}\right]_{27}$ of the curves for sucrose, fructose and grape juice are 69.59, 92.13 and 93.19 respectively where the subscript 27 refers to the temperature at which the experiment was done.

3.2. Study of variation of optical rotation with concentration for different wavelengths of light

The graph of refractive index against concentration is a straight line as shown in figure. Given a solution with an

unknown concentration, its refractive index can be determined experimentally. The graph can be extrapolated or interpolated to determine its concentration. The gradients $\left[\frac{dn}{dc}\right]_{27}$ of the curves for sucrose, fructose and grapes juice are 0.137, 0.114 and 0.23 respectively. Using the equation of the straight line the concentration can also be determined where the intercept is

For sucrose = 1.333
For fructose= 1.335
For grapes juice =1.328
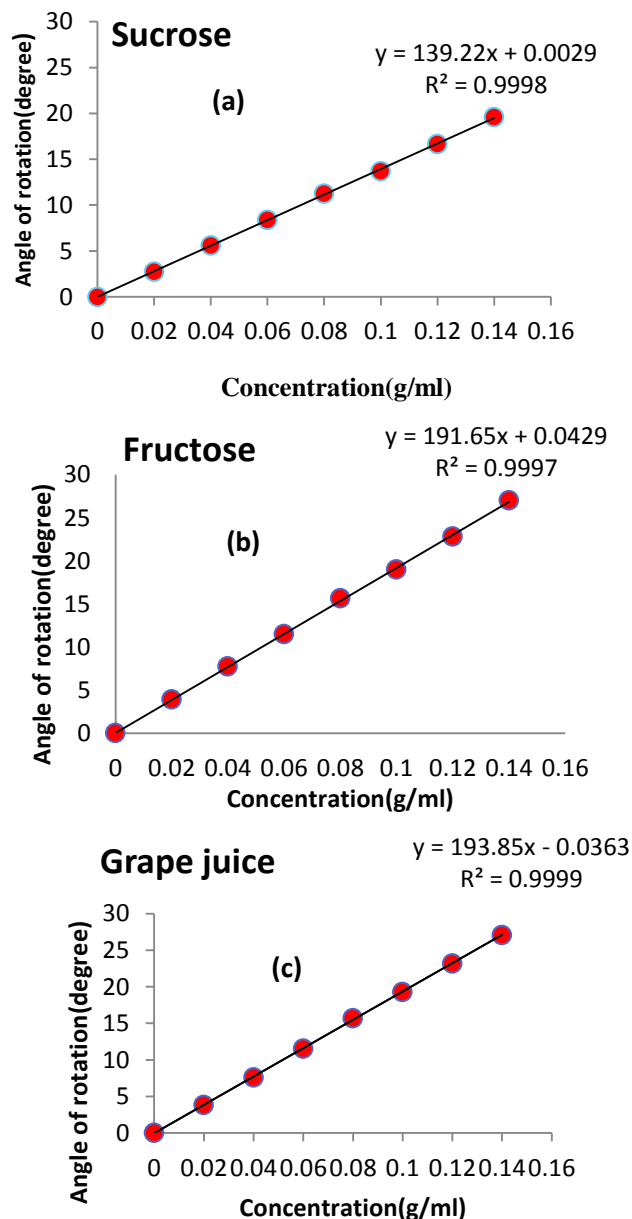
Figure 4 (a), (b) & (c): A graph of angle of optical rotation versus concentration for sucrose, fructose solutions and grape juice respectively using Sodium-D-Lamp.
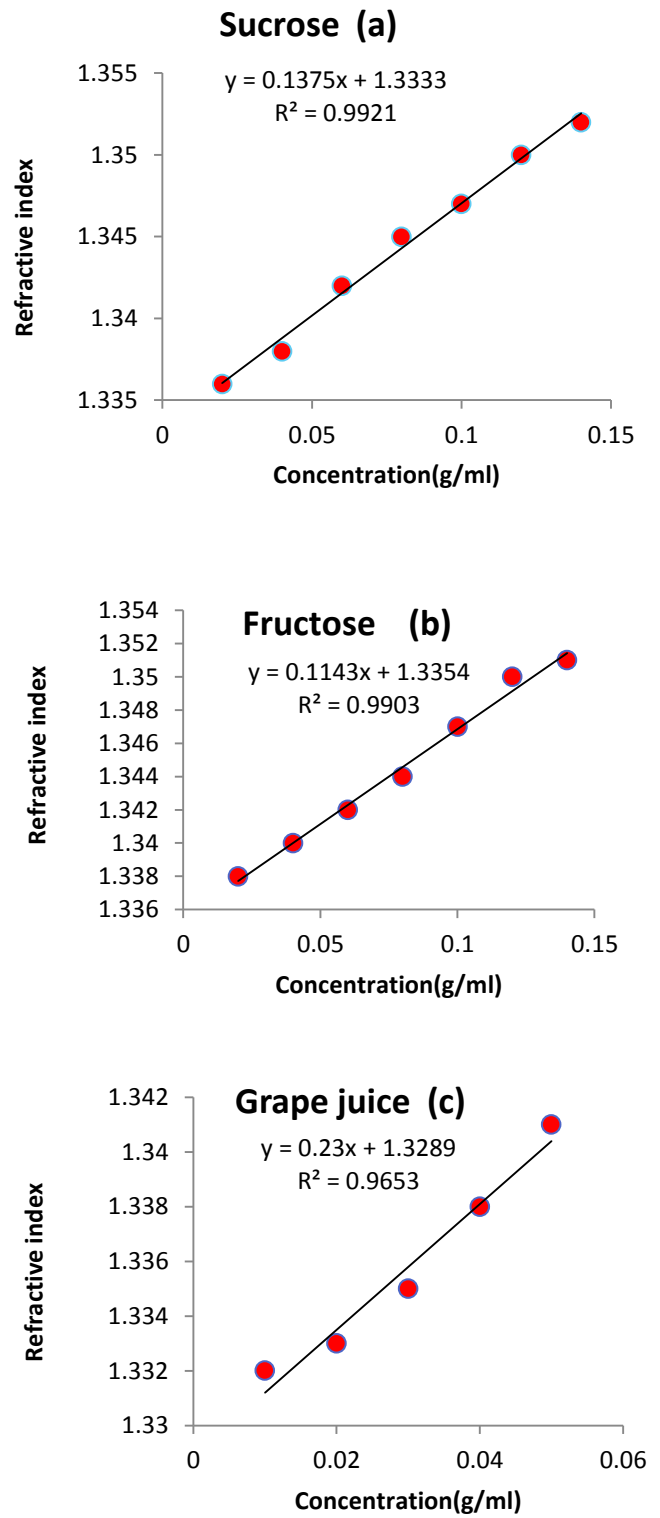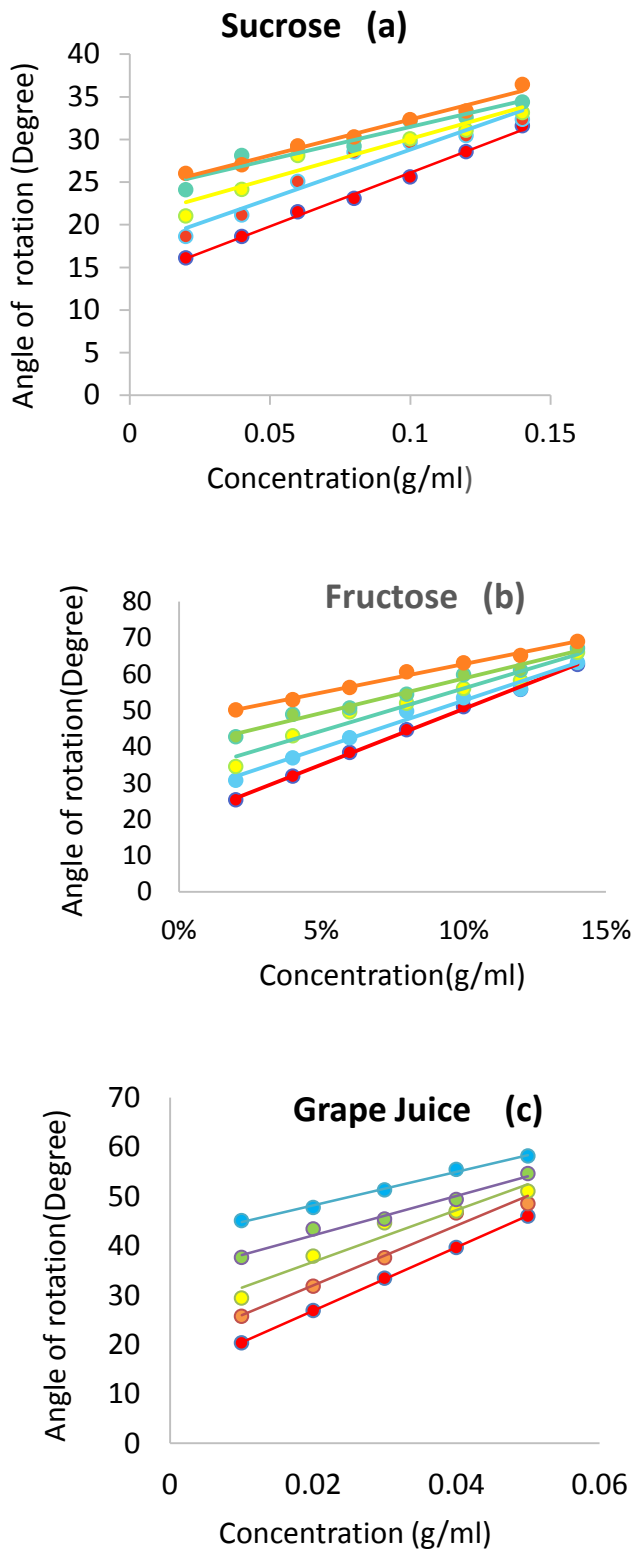
Figure 5 (a), (b) &(c): A graph of angle of optical rotation versus concentration [for different wavelengths] for sucrose, fructose solutions and grape juice respectively.

Figure 6 (a), (b) & (c): A graph of angle of refractive index versus concentration for sucrose, fructose solutions and grape juice respectively using Sodium-D-Lamp.

The optical angles of rotation of Sucrose and fructose plotted in Figure 4[a,b] are obtained from sucrose and fructose solutions ranging in concentrations from zero to 0.16 g/ml with an increment of 0.02g/ml and yield values of specific rotational angle for sucrose and fructose of 69.59 degree and -92.64 respectively. These observations of 69.59 and -92.64 degrees are in reasonable agreement with the reference specific optical rotation value for sucrose of 66.49 degrees [5]. Moreover, the optical angles of rotation of grape juice plotted in Figure 4 (c) are obtained from grape juice ranging in concentrations from zero to 0.05 g/ml with an increment of 0.01g/ml and yield a specific rotational angle value for grapes juice of -92.74 degree. The quality of the results is good with R2 value 0.999.

The variation of angle of rotation and concentration for different wavelengths [Figure 5(a)&(b)] obtained for sucrose and fructose solutions ranging in concentrations from zero to 0.14 g/ml with an increment of 0.02g/ml indicates that the effect of polarized solution on the rotation angles is more with decrease of wavelength. It is noted that higher sensitivity is possible for sucrose detection by using polarimetric method at a shorter wavelength.

The variation of refractive index (n) with concentration (g/ml) of sucrose and fructose was studied by plotting graphs as shown in Figure [6(a) & (b)]. From the graphs the linear dependence of refractive index (n) with concentration (g/ml) is evident and the values of refractive index increase with increasing concentration. The variation of refractive index (n) with concentration (g/ml) of grape juice was studied by plotting the corresponding graph shown in Figure [6(c)], which also indicates that the values of refractive index increase linearly with increasing concentrations. The quality of the results is good with R2 value ranging from 0.990-0.996.

4. Conclusions:

An innovative, simple and economic technique was used to determine the optical property, refractive index of the known concentration of transparent sucrose and fructose solution and raw grapes juice. Experiment showed that optical method could be safely employed to study the dependence of angle of rotation of solutions on their concentration as well as refractive index. Linear dependence of angle of rotation of sucrose, fructose and raw grapes juice on their concentration at different

wavelength with their concentrations was observed and the values and trend were in agreement with the literature. Moreover the linear dependence of refractive index of sucrose, fructose and raw grapes juice with their concentrations was also observed. This method is used in determination of sugar concentration of solutions which is useful for treatment of diabetic patients. This method is used to analyze the sugar purity and content using a polarimeter.

5. Acknowledgement:

6. References

[1] D.J Matti, *Engineering Journal (NUCEJ),* 17 (2014) 60-66.

[2] Haliday D.; Resnick, R. Walker, J. *Fundamental of Physics-6th Edition*, 2001

[3] https://courses.lumenlearning.com/physics/chapter/28-8-porisation/

[4] F.J. Bates et al.: *Polarimetry, Saccharimetry and the Sugars. National Bureau of Standards, Washington D.C.* 1942.

[5] T. Dhliwayo, Application of optical methods to determine the concentration of sugar solutions.

Bulletin of Physics Projects

Journal homepage: http://www.bbcphysics.in/index.php/journal

Study of elevation of Boiling point of distilled water in presence of different salts of chlorides

Debajyoti Dutta, Priyanka Bhattacharjee, Shyam Kumar Das, Smritimala Sarmah[#]
Dept. of Physics, B. Borooah College
[#] Corresponding author's e-mail address: smritimala@gmail.com

Abstract

In this work, the effect of ionic salts on boiling point of distilled water has been studied using platinum resistance thermometer. Three non-volatile ionic salts viz. ammonium chloride, sodium chloride and potassium chloride of different molar concentrations have been dissolved individually in distilled water. Boiling point of each solution has been measured. In all three salt solutions, boiling point increases with the increase in solute concentrations in distilled water, showing the same trend which indicates that boiling point depends on the molar concentration of the solute. Boiling points of distilled water slightly increases in case of increasing molecular weight of the solute.

1. Introduction

Boiling point is an essential part of living for humans on earth. It is seen that liquids that contain dissolved substances have increased boiling points. For example the ocean, which has 3.5% salt has boiling point between 115^0C to 120^0C depending on the salinity of water. This is a significant increase, when compared to the boiling point of pure water (100^0C).This effect is called boiling point elevation. Now, boiling point of a liquid is the temperature at which the vapour pressure of the liquid becomes equal to the external pressure, exerted on it. The main reason for the increase in the temperature of the boiling point is colligative property of the solution. Colligative properties refer to the property of the solution that is dependent only on the concentration of the solute particles in the solution. Colligative properties change in proportion to the concentration of the solute particles. Colligative properties

are distinguished in four ways: vapour pressure, freezing point, depression, boiling point elevation and osmotic pressure [1].

Vapour pressure is the pressure exerted by the vapours released by a liquid or solid substance in a closed space. When water boils, the molecules are able to overcome the vapour pressure of the surrounding air to move from the liquid phase to the gas phase. But in the presence of a solute, the vapour pressure decreases, and hence the water molecules cannot easily escape from liquid phase to gas phase. Water boils when the molecules are able to overcome the vapour pressure of the surrounding air to move from the liquid phase to the gas phase. When a solute is added to water, a few different processes occur that increases the amount of energy (heat) needed for water to make the transition. Meranda et al studied elevation of boiling point of water using 40

different salts [2]. They found that boiling point increases for all the salts present in saturation in boiling water. Dan et al. measured the elevation of boiling point for urea water solution with respect to urea mole fraction [3]. Romero et al measured the rise in boiling point of coffee extract prepared in distilled water at different soluble solids concentrations [4].

In this work, we have studied the elevation of boiling point of distilled water with three different ionic salts using platinum resistance thermometer.

2. Experimental Details

Sodium chloride (NaCl) (Merck), ammonium chloride (NH_4Cl) (Merck) and potassium cholride (KCl) (Merck) was used without further purification. Five different concentrations NH_4Cl solution in distilled water were prepared. The boiling points of the solutions were measured using platinum resistance thermometer. Similar procedure was followed for NaCl and KCl.

3. Results and Discussions

Boiling point of distilled water was measured using platinum resistance thermometer. It was found to be 100^0C. Variation of boiling point of distilled water in
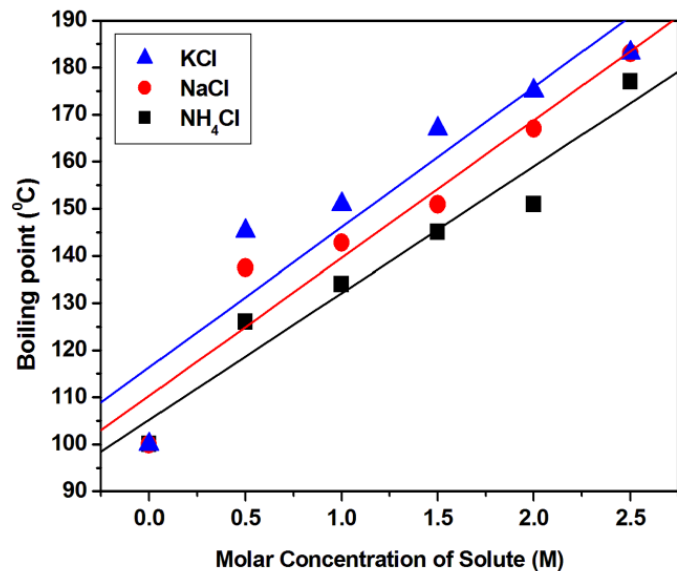
Figure 1: Variation of boiling point with molar concentrations of NH_4Cl, NaCl and KCl.

presence of different molar concentrations of NH_4Cl is shown in Fig. 1. It is observed from the figure that the boiling point of distilled water is increasing linearly with the increase in molar concentration of NH_4Cl. Similar characteristics are observed in case of distilled water solutions containing NaCl and KCl. When an ionic salt is

added to water; it dissociates into ions. These charged particles alter the intermolecular forces between the water molecules. Every water molecule is a dipole. The positively charged ion aligns with the oxygen side of a water molecule, while the negatively charged ion aligns with the hydrogen side of the water molecule. The ion-dipole interaction is stronger than the hydrogen bonding between the water molecules, so more energy is needed to move water molecules into the vapour phase. Adding any solute raises the boiling point of water because part of the pressure the solution exerts on the atmosphere now comes from solute particles as well and not just the solvent (water) molecules. The water molecules need more energy to produce enough pressure to escape the boundary of the liquid phase. The more the salt (or any solute) added to water, the more is the raise in boiling point. This phenomenon depends upon only the no. of solute particles in the solution.

In Table 1, the boiling point of water solution all three salts with concentrations 0.5 M and 2.5M and the molecular weights of the salts are given. It is observed, that the values of boiling points for both concentrations of

Table I

Dependence of boiling point of water solution on the molecular weight of solutes

Sl. No.	Salts	Molecular weight (g/mol)	Boiling point in ^{0}C for	Boiling point in ^{0}C for
			0.5 M	2.5 M
1.	NH_4Cl	53.5	126	177
2.	NaCl	58.44	137.5	183.1
3.	KCl	74.55	148.25	185

solutes are following a particular trend with the molecular weight of the salts. Higher the molecular weight of the salt, more is the boiling point of distilled water solution. Substances boil when the attractions between molecules are overcome by the energy of thermal motion. Smaller molecules have greater thermal motion, on average, than big molecules because kinetic energy is proportional to mass and the square of velocity. So, in general, smaller molecules have a lower boiling point. Thus the boiling

point in NH$_4$Cl solution is smaller as compared to NaCl and KCl solution for the same molar concentration [1, 5].

4. Conclusions

In this work, the elevation of boiling points of distilled water in presence of three ionic salts has been studied using platinum resistance thermometer. It is found that boiling point of water increases linearly with the increase in concentration of solutes. Boiling points of water slightly increases in case of increasing molecular weight of the solute.

6. References

[1] P. W. Atkins, *Physical Chemistry*, 4th Ed., Oxford University Press, Oxford, 1994, ISBN 0-19-269042-6, p. 222-225

[2] D. Meranda and W. F. Furter, *J. Chem. Eng. Data*, 22 (3) (1977), 315–317

[3] H. J. Dan and J. S. Lee, *J Mech Sci Technol.*, 30 (2016), 1443-1448

[4] J. Telis-Romero, R. A. F. Cabral, G. Z. Kronka and V. R.N. Telis,.*Braz. J. Chem. Eng*. 19(1) (2002), 119-126

[5] R. Rich,J. *Chem. Edu. 39* (9) (**1962**), 454-460

Bulletin of Physics Projects

Construction of an Affordable SRT and Demonstration of Some Basic Radio Astronomy Techniques

Sasanka Talukdar, Bitopan Ray, Kaushik Saikia, Diganta Kumar Sarma[#]

Department of Physics, B. Borooah College

[#] Corresponding author's e-mail address: sarma.diganta@gmail.com

Abstract

The conversion of a satellite television dish antenna into a small radio telescope (SRT) and some of its basic applications are studied here. The beam width of the antenna is measured and compared with the theoretical value. The results show good agreement. The SRT is then used to observe relative solar flux density and flux density from some geostationary satellites for the period from 6th March to 28th March, 2018. The data shows that the solar flux density varies with time but the flux density from geostationary satellites remains relatively steady. The telescope is then used create a radio image of the sky. From the image developed ten numbers of geostationary satellites and their clark orbit could be able to identify. Flux density from INSAT 3A is observed during rainy situation. The flux density observed to be increased for rainy situation.

1. Introduction

A radio telescope is a specialized antenna and radio receiver used to receive radio waves from astronomical radio sources in the sky. Just as an optical telescope uses the visible light of the electromagnetic spectrum to observe distant objects, radio telescope uses radio waves to do the same. Radio telescopes are typically large parabolic dish antennas similar to those employed in tracking and communicating with satellites and space probes. Radio waves from space were first detected at Bell Telephone Laboratories in Holmdel, New Jersey [1] using an antenna built to study noise in radio receivers.

Radio frequencies vary from 300GHz to 3KHz, and corresponding wavelengths from 1 millimeter to 100 kilometers. Because of its long wavelengths, radio waves can travel vast distances without getting scattered. It is very suitable for astronomy because radio telescopes can be installed anywhere since the earth's atmosphere does not affect radio waves.

But building a radio telescope can be very costly because they require different sophisticated equipment and electronics. Our main objective of this project is to build a affordable small radio telescope(SRT) using easily available items and use it to perform some basic radio astronomy experiments. Kalinova V. 2011 [2] has made solar observations in 1.4 GHz using a SRT. Here we are going to use a satellite TV dish antenna for the telescope. The LNB attached to a regular satellite dish can be used to observe synchrotron radiations as shown by Caspers F. et al. 2011 [3] at CERN.

The Sun is one of the strongest radio sources in the sky. The Sun emits radio waves since it's hot (it is said that, thermal sources emits radio waves at high frequencies). But there is a strong emission even at lower frequencies because of the mechanism of synchrotron radiation which derives from the movement of high speed electrons around the magnetic field.

The solar radiation spectrum covers all frequencies ranging from radio to optical. The solar radiance and temperature are a function of the wavelength. In the optical range (100-nm to 1000-nm wavelength), the Sun can be treated as a blackbody with a constant temperature of about 6000 K. The radiation flux is quite stable, with very small changes over the solar cycle. However, in the radio frequency band (1 cm to 30 cm wavelength, approximately), the radiance for a disturbed Sun and for a quiet Sun is significantly different from that of the blackbody in the optical range. The spectral density becomes much greater than at longer wavelengths for both a quiet and disturbed Sun and these elevated fluxes come mainly from the contribution of the solar corona and the chromospheres. Radio emission at meter- and decimeter-wavelengths from flares is quite different from emissions at centimeter and millimeter wavelengths. This has to do with the fact that at the shorter wavelengths the emission is caused by incoherent gyro-synchrotron radiation mechanisms while at the longer wavelengths the emission comes from coherent plasma radiation. The 1-3 GHz frequency range appears to lie at the transition between the two types of emission mechanisms.

The solar atmosphere emits radio emission at all wavelengths and at all times. Its total flux density varies with magnetic activity as manifest in sunspots. At every wavelength there is a well-defined minimum radiation level. It is reached when the sun has been free of spots for some weeks. This is called the quiet radio emission of the sun. The presence of sunspots enhances the radio emission, producing a slowly variable component.

The basic objectives of the present work are (a) To build a small radio telescope (SRT) using a TV dish antenna, (b) Measure the half power beam-width of the SRT using the sun as a point source, (c) Use the SRT to observe the sun and measure the variations in relative solar flux density throughout a month, (d) Use the SRT to observe the satellites in the geostationary orbit and create a radio image of the sky and (e) Use the SRT to observe the variation of radiation observed from a satellite in rainy situation.

2. Experimental Details

2.1 Methodology:

The methodology adopted in the present study is depicted as the schematic diagram in figure 1. Figure 1 shows the step by step procedure for the present study. Started with the assembly of the dish is followed by installation of angle measuring scales, measurement of half power beam width and application in different fields.
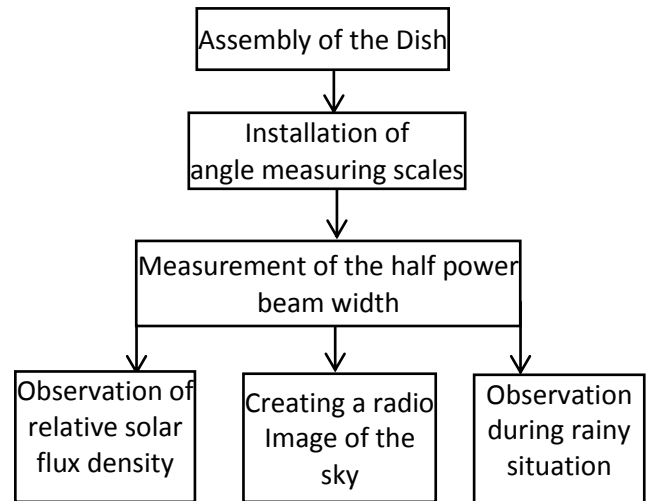
Figure 1: Schematic diagram of the methodology

2.2 Measurement of the beam-width

The process involves letting the earth's rotation act as rotator to move the dish at a known rate. To measure the half power beam-width of the dish, it is pointed towards the path of the sun in the sky and the multimeter readings in a time interval of 30 seconds is recorded. As time passed, the sun crossed the beam of the dish and a maximum reading is obtained. Knowing the angular velocity of the sun in the sky, the half power beam-width is calculated from the time taken for the sun to cross the two -3dB points.

2.3 Observation of relative solar flux density

The relative solar flux density is observed by pointing the dish directly at the sun at a particular time of the day (around 3.15 pm). After that the flux density of two known geostationary satellites are measured without changing the attenuation value in the satellite finder to take them as reference as they are always constant. The readings are taken for around twenty days in the month of March.

2.4 Creating a radio image of the sky

A radio telescope measures the intensity of radio waves emitted from the part of the sky where it is pointed to. By aiming our telescope at different parts of the sky, we measured the different intensities and then converting the data into different shades of colour, a radio image is obtained.

Figure 2: Taking data for creating a radio image.

2.5 Instrumental Information:

Figure 3 below shows the schematic diagram of the different components of the SRT.
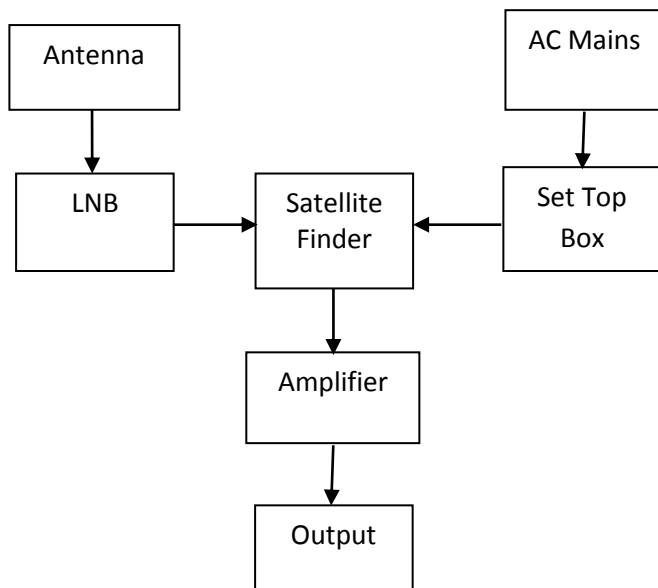
Figure 3: Schematic representation of the components of the SRT

2.5.1 Parabolic Antenna:

The job of the parabolic antenna is to focus the parallel beams falling on the dish to a single point thus increasing the intensity of radio signals received by the LNB. We have used a standard satellite tv dish antenna for this purpose. The diameter of our dish is 60 cm. Also the dish we used is a 22 degree offset dish. The 22 degree offset means that the beam comes off the dish at an offset angle of 22 deg. So, with the feed arm at the bottom, if the front face of the dish reflector itself is vertical, the beam

elevation angle is 22 deg upwards. Because of this feature, to aim the dish at a particular target, the dish should be elevated 22 degrees upward than the original position.
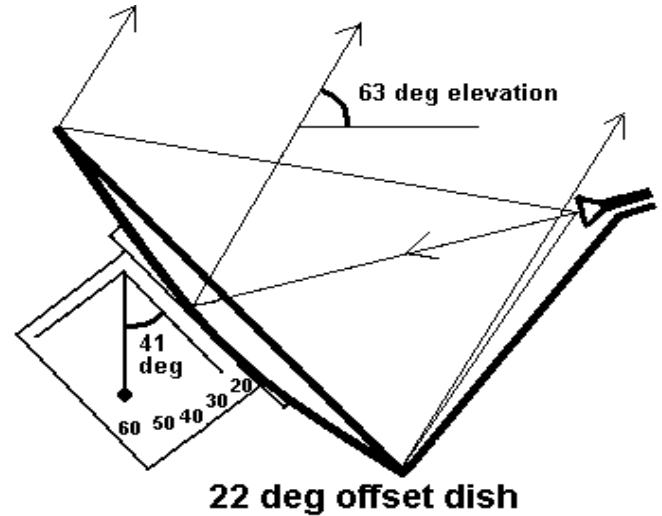
Figure 4: Schematic diagram of a 22° offset antenna

2.5.2 Disc Mount:

We have used standard dish mount as stand for the dish. The dish is mounted on top of a bicycle wheel ring. Then the circumference of the ring is divided into 360 equal parts so that it can be used to measure the horizontal angle of the dish. To accurately measure the vertical angle, first it was made sure, that the dish was pointed at 0º, by using a spirit level. Then a small weight is hanged from the pivot point using a thread. After that, a protractor is stuck in such a way, that the thread matches with the 0º angle on the protractor. Now when the dish is rotated vertically, the thread always shows the exact angle of the inclination of the dish.
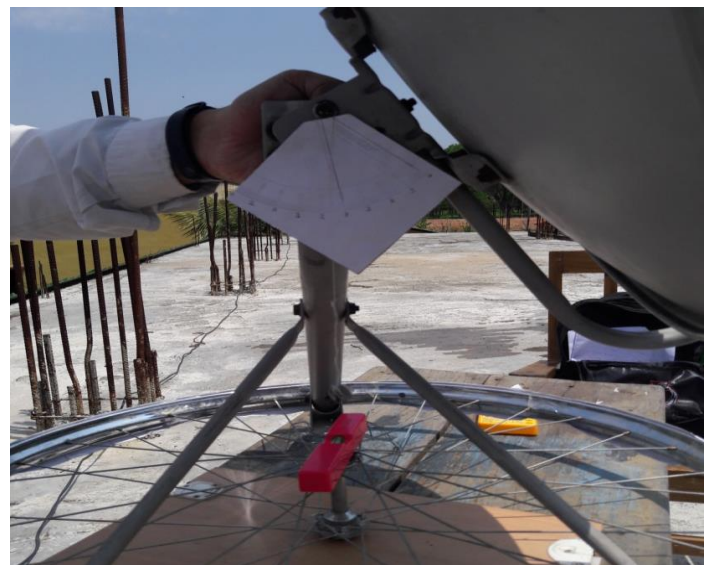
Figure 5: Scale for measuring the inclination of the dish

2.5.3 Low-Noise Block Down converter (LNB):

The abbreviation LNB stands for Low Noise Block. It is the device on the front of a satellite dish that receives the very low level microwave signal from the satellite, amplifies it, changes the signals to a lower frequency band and sends them down the cable to the indoor receiver.
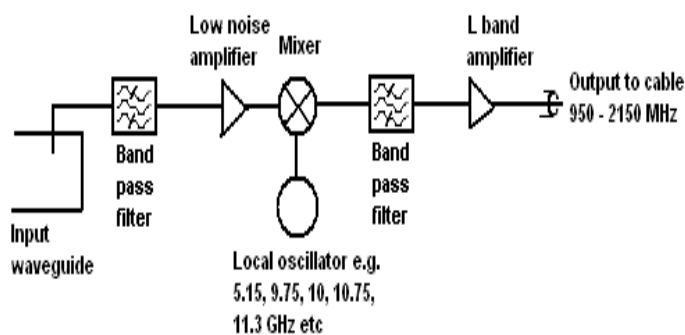
Figure 6: Low noise block down converter (LNB)

The diagram shows the input waveguide on the left which is connected to the collecting feed or horn. As shown there is a vertical pin through the broad side of the waveguide that extracts the vertical polarization signals as an electrical current. The satellite signals first go through a band pass filter which only allows the intended band of microwave frequencies to pass through. The signals are then amplified by a Low Noise Amplifier and then to the Mixer. At the Mixer all that has come through the band pass filter and amplifier stage is severely scrambled up by a powerful local oscillator signal to generate a wide range of distorted output signals. These include additions, subtractions and multiples of the wanted input signals and the local oscillator frequency. Amongst the mixer output products are the difference frequencies between the wanted input signal and the local oscillator frequencies. These are the ones of interest. The second band pass filter selects these and feeds them to the output L band amplifier and into the cable. Typically the output frequency = input frequency - local oscillator frequency. In some cases it is the other way round so that the output frequency = local oscillator frequency - input frequency. In this case the output spectrum is inverted.

Here, a universal LNB with a input frequency band 10.7-11.7 GHz is used. It has a local oscillator of 9.75 GHz and

produces an intermediate frequency (IF) of range 950-1950 MHz.

2.5.4 Satellite Finder:

The output from the LNB is feed to a satellite finder which detects the power of the signal. We are using a **MX-467A** satellite finder, which uses an analog dial to show the power of the radio signal. The satellite finder measures the amount of RF energy over a wide frequency range by summing the power from all transponders and producing Received Signal Strength Indicator output, by means of proportionate DC voltage which is then supplied to an analog galvanometer dial. Our satellite finder has an input frequency range of 900 MHz -2150 MHz.

Figure 7: Satellite finder
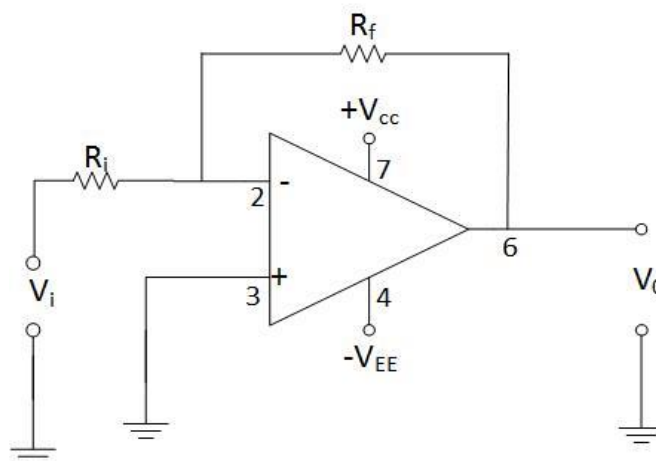
Figure 8: Schematic diagram of the amplifier circuit

2.5.5 Amplifier circuit:

We found that the small dial on the satellite finder is not accurate enough for measuring the small variations of signal strength. So, we decided to directly measure the DC voltage across the two terminals of the galvanometer in the
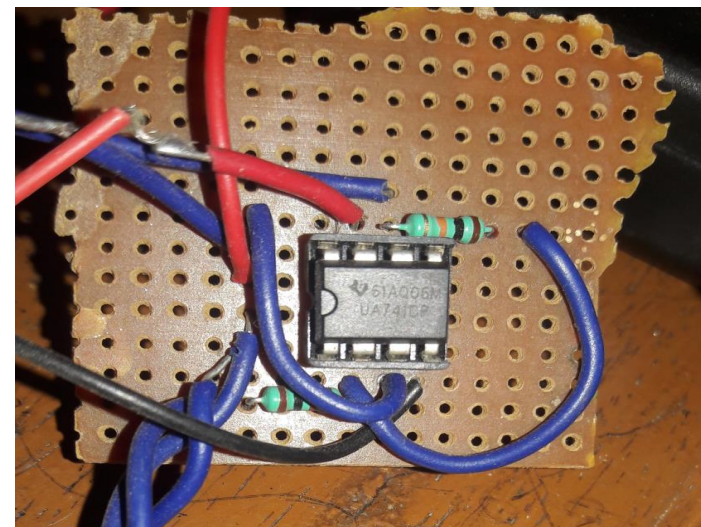
Figure 9: Amplifier circuit using 741 OPAMP

satellite finder by amplifying it with a op-amp amplifier circuit. Opamp stands for operational amplifier. Its an
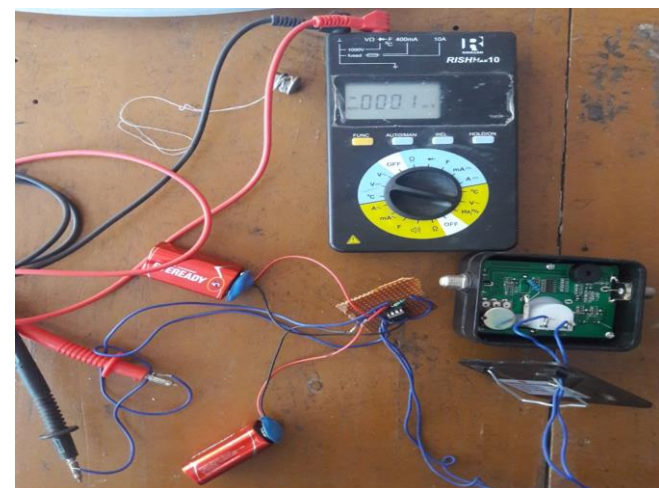
Figure 10: Measurement of output voltage from Amplifier circuit

integrated amplifier circuit which operates on differential mode. We have used a basic inverting amplifier using an OP AMP(IC 741) connected with an input resistance R_i=1K ohm and and a feedback resistance R_f=10K ohm. Since R_f connects the output terminals to the inverting input terminals, it provides a negative feedback. The non-inverting terminal is grounded. We used two 9 volt batteries to provide the biasing potential for the op amp

circuit. After amplification, the output DC voltage signal from the amplifier circuit is measured by a digital multimeter.

3. Results and Discussions:

3.1 Measurement of half power beam width:

Before our radio telescope is used for any kind of observation, we should first know about the beam width of the dish. The beam width value will give an idea about the resolution of our dish. The theoretical value of half power beam width (HPBW) of a parabolic antenna is given by the formula, $\theta_t=70\lambda/d$. In our case, the diameter of our dish, d=60 cm and the wavelength received by the dish, λ=2.56-2.80 cm. So, the theoretical value of HPBW is $\theta_t = 3.12667^o$. As discussed in the methodology section, the beam width is measured. Then it is compared with the theoretical value.

Table I

Multimeter reading in time domain

Sl. No.	Time (min)	Multimeter Reading (Volt)	Sl. No.	Time (min)	Multimeter Reading (Volt)	Sl. No.	Time (min)	Multimeter Reading (Volt)
1	0.0	0.511	17	8.0	2.443	33	16.0	2.312
2	0.5	0.553	18	8.5	2.482	34	16.5	2.253
3	1.0	0.654	19	9.0	2.535	35	17.0	2.176
4	1.5	0.883	20	9.5	2.568	36	17.5	2.080
5	2.0	1.068	21	10.0	2.606	37	18.0	1.981
6	2.5	1.302	22	10.5	2.621	38	18.5	1.883
7	3.0	1.489	23	11.0	2.632	39	19.0	1.766
8	3.5	1.627	24	11.5	2.641	40	19.5	1.640
9	4.0	1.757	25	12.0	2.625	41	20.0	1.482
10	4.5	1.878	26	12.5	2.607	42	20.5	1.307
11	5.0	1.988	27	13.0	2.594	43	21.0	1.102
12	5.5	2.065	28	13.5	2.563	44	21.5	0.864
13	6.0	2.158	29	14.0	2.527	45	22.0	0.617
14	6.5	2.235	30	14.5	2.482	46	22.5	0.513
15	7.5	2.371	32	15.5	2.388	48	23.5	0.516
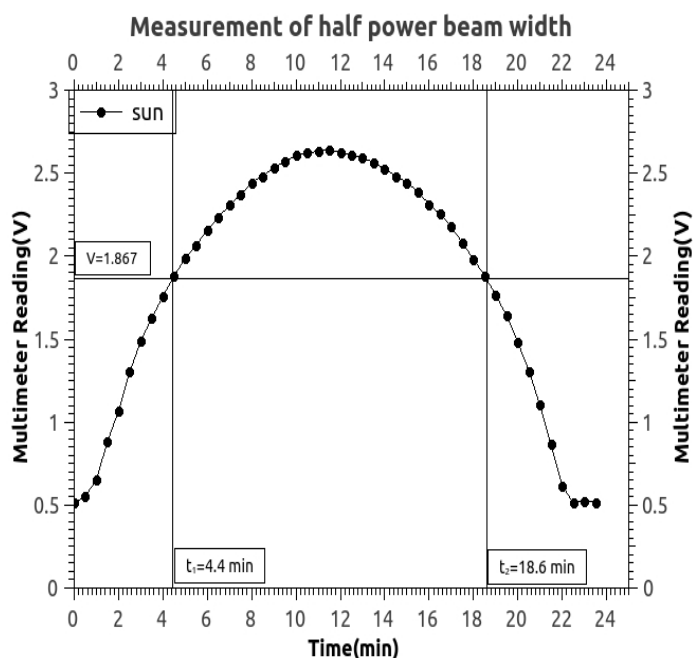
Figure 11: Measurement of half power beam width

From figure 11, The peak value of voltage, V_o=2.641V

So, the half power value is given by,

$$V_{half} = \frac{V_o}{\sqrt{2}} = 1.867 \text{ V}$$

The time taken for the sun to cross the two -3dB points, $\Delta t = t_2 - t_1 = (18.6-4.4)$ min =14.2 min

The sun travels 360 degrees in the sky in 24 hours.

So, the angular velocity of the sun,

$$\omega = \frac{360}{24*60} = 0.25^o/minute$$

So, the practical value of half power beam width of our dish is, $\theta_p = \omega * \Delta t = 3.55^o$

So, it is seen that the theoretical value and the practical value of half power beamwidth of our antenna are very close to each other. But the beam width of our antenna is quite large comparing to other sophisticated radio telescopes, which indicates a very low resolution capacity of our telescope. So, it not possible to use our dish for advance astronomical studies. But it can be used to demonstrate some basic radio astronomy techniques.

3.2 Observation of relative solar flux density:

Solar flux density means the mean solar electromagnetic radiation per unit area. It is measured in the unit of W/m². The satellite finder in our radio telescope measures the power of the input signal and converts it to an equivalent

DC value. So, it gives us a relative measure of the solar flux density. We can then use it to observe the variations of solar flux density. The relative solar flux density is measured by pointing the dish directly at the sun at a particular time of the day (around 3.15 pm). After that the flux density of some known geostationary satellites (Insat 3A, AsiaSat5) are measured without changing the attenuation value in the satellite finder to take them as reference since they are always constant. The readings are taken for around twenty days in the month of March.

Table II
Observation of relative solar flux density

Sl. No.	Date	Multimeter Readings (volts)		
		Sun	INSAT 3A	AsiaSat 5
1	6.3.18	2.164	2.993	2.516
2	7.3.18	2.118	2.981	2.519
3	8.3.18	1.904	2.984	2.503
4	9.3.18	1.822	2.978	2.528
5	10.3.18	2.056	2.990	2.532
6	12.3.18	2.112	2.993	2.507
7	13.3.18	2.264	2.984	2.526
8	14.3.18	2.215	3.015	2.506
9	15.3.18	2.098	2.991	2.498
10	16.3.18	2.031	2.983	2.519
11	17.3.18	2.255	2.987	2.510
12	19.3.18	2.345	2.995	2.518
13	20.3.18	2.482	2.979	2.526
14	21.3.18	2.317	2.983	2.500
15	22.3.18	2.269	3.016	2.532
16	23.3.18	2.237	2.971	2.530
17	24.3.18	2.187	2.984	2.516
18	26.3.18	2.263	2.988	2.521
19	27.3.18	2.223	2.991	2.509
20	28.3.18	2.293	2.993	2.515

Figure 12 show that, the value of solar flux density varies daily while the flux density of the satellites remained relatively steady. This result tells us about the nature of solar emission in the radio wavelength region. In the radio

frequency range, the Sun has both slowly varying and rapidly varying components. The long-term variations include annual and 11-year solar cycle variations, while short-term variations usually mean changes within days. These variations of solar flux density represent the ever changing magnetic field of the sun, since radio waves in the centimetre region are mainly produced due to synchrotron radiation of the sun.
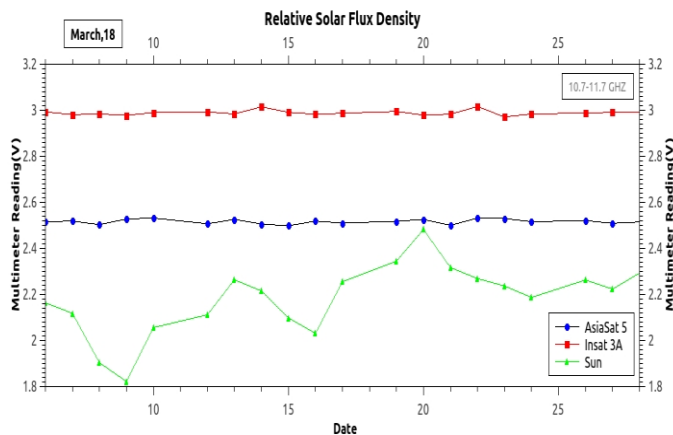
Figure 12: Diurnal variation of solar flux density

It is worth noticing that, the apparent intensity of both the satellites is higher than the sun. It is due to the fact that, though sun produces a much more powerful radio emission, it is very far apart from earth and it radiates in all directions. This means the intensity of the wave decreases according to the inverse square law. On the other hand, the satellites are very near to the earth's surface and they produce a highly focused beam of radio wave. That's why each satellite can only operate for a very small region on earth and for different regions we need different satellites.

3.3 Creating a radio image of the sky:

As mention in the methodology, we tried to create a radio image using our radio telescope. We scanned the sky from vertical angle 20° to 70° and horizontal angle 0° to 180°, at intervals of 1^O and stored the data in a [50*180] matrix. After that we convert the matrix to a gray shade image using QtiPlot software. Every white dot in Figure 13 represents a radio source, or in this case a geostationary satellite. Here we can easily notice the geosynchronous orbit in the sky. Though the image is not very detailed due to the telescopes low resolution, it demonstrates how radio imaging telescopes create radio images of different deep space objects, which would be otherwise invisible to us. The brightness of each pixel represents the radio intensity.

The bright dot in the middle is Insat 3A which used for DD Direct Plus[4]. From the internet[4] we were able to get the list of different geostationary satellites for India and their azimuth angles. By comparing them with our data, we were able to identify some of the satellites in the image. They are-

1. Intelsat 906
2. Eutelsat W5
3. Insat 4CR (Airtel DTH)
4. Insat 4A (Tata Sky)
5. ST 1 K2 (Videocon D2H)
6. Insat 3A/4b (DD Direct Plus, SUN Direct HD)
7. NSS 6 (Dish TV)
8. AsiaSat 5
9. AsiaSat 3S
10. SES 7 (Airtel DTH)
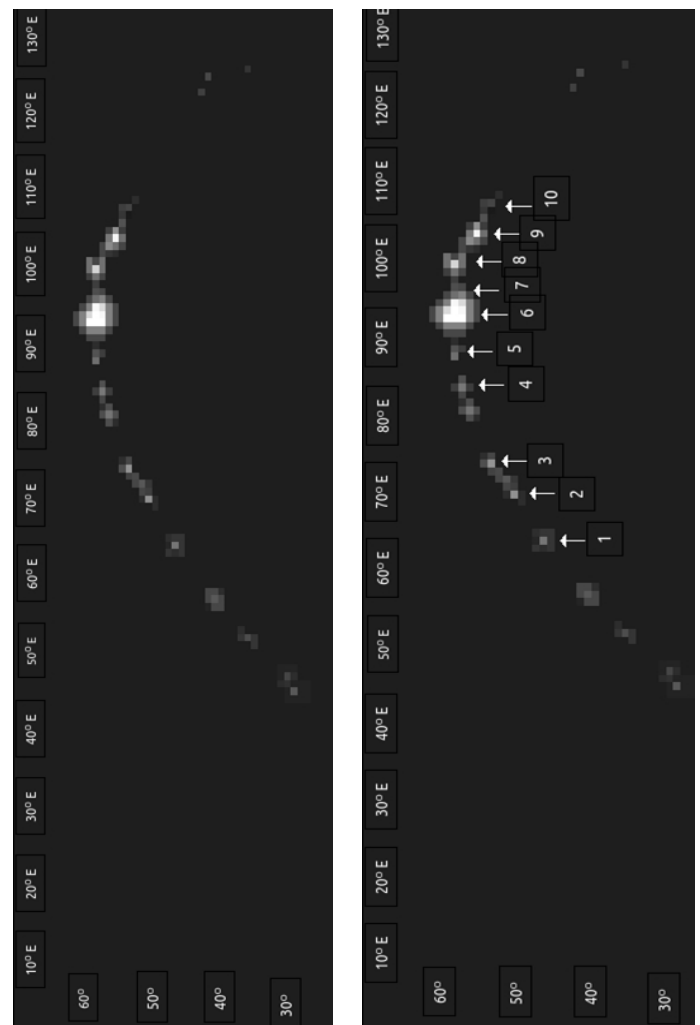
Figure 13: Constructed radio images for different satellite

3.4 Flux density during rainy situation:

The SRT developed is use to measure the flux density during cloudy/rainy condition. For that purpose the data received from INSAT 3A is considered. The reading was taken from the beginning to the end of a rain event on 16.03.2018. In the beginning, the intensity of the rain was maximum and decreases rain gradually with time.

Table III

Flux density observed during rainy situation for INSAT 3A
Rain Starting time: 1.51 pm Rain Ending time: 2.23 pm

Sl. No.	Time (pm)	INSAT 3A Reading (V)
1	1:51	3.254
2	1:52	3.256
3	1:53	3.252
4	1:54	3.248
5	1:55	3.251
6	1:56	3.246
7	1:57	3.237
8	1:58	3.221
9	1:59	3.235
10	2:00	3.242
11	2:01	3.215
12	2:02	3.197
13	2:03	3.183
14	2:04	3.175
15	2:05	3.167
16	2:06	3.157
17	2:07	3.134
18	2:09	3.119
19	2:11	3.117
20	2:13	3.112
21	2:15	3.109
22	2:17	3.105
23	2:19	3.098
24	2:22	3.094
25	2:24	3.073
26	2:26	3.074

Figure 14 shows that the reading from the satellite had a maximum value at the start of the rain and it decreases as the intensity of the rain deceases. It is because of the fact that during rain, radiation emitted from the cloud and rain is added with the satellite signal. The SRT developed can detect radiation from any object in the region 10.7-11.7 GHz. Thus it can be inferred that at this frequency range the received radiation is more in rainy situation compared to the non-rainy situation.
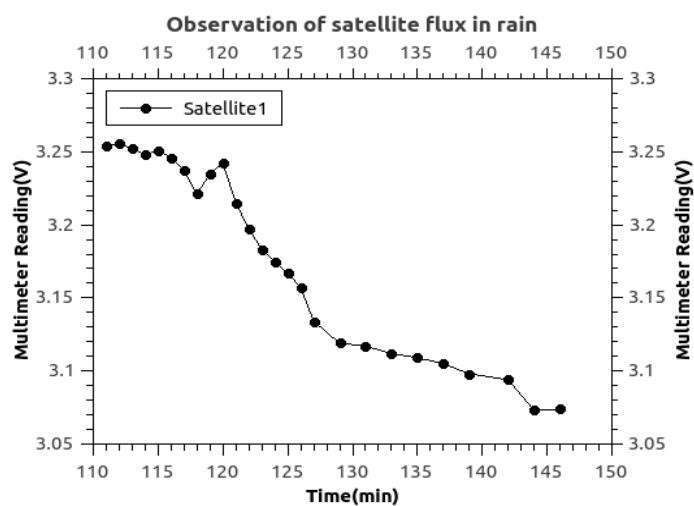
Figure 14: Variation of flux density during rainy condition on 16.03.2018

4. Summary and Conclusions

This project deals with the construct of a small radio telescope using a regular dish antenna and demonstrated some basic radio astronomy techniques viz.

- A small radio telescope is built using a TV dish antenna.
- The half power beam width of our antenna is measured and then compared with the theoretical value.
- The variation of solar flux density is observed.
- A radio image of the sky is constructed in which we have observed some geostationary satellites.

From this project the following conclusions are drawn:

- It is possible to build a radio telescope using a satellite tv dish. This can perform basis radio observations.
- The half power beam width of the telescope can be measured by using the sun. The measured value shows good agreement with the theoretical value.

- The solar flux density varies with time but the flux density from artificial satellites remains relatively steady.
- All the geostationary satellites are in the same geostationary orbit and their positions always remains the same.
- During rainy situation the flux density observed to be different from the non rainy situation. The flux density received by the SRT is high during rainy situation.

5. Acknowledgement:

6. References

[1] Jansky K G., Electrical disturbances apparently of extraterrestrial origin, Proc. IRE 21:1387-98, 1933

[2] Kalinova V., Solar observations with the Small Radio Telescope, 2011

[3] F. Caspers et al., Observation of synchrotron radiation using Low Noise Block (LNB) at ANKA, CUPD39, 2011

[4] https://dreamdth.com/threads/all-ku-band-satellites-recivable-in-india-official-coverage.5160/

[5] http://www.ncra.tifr.res.in/rpl/faqs/extra-information/affordable-small-radio-telescope/asrt.pdf

[6] Beamwidths and Sidelobe Levels http://www.antenna-heory.com/basics/radPatDefs.php

[7] Benz A O, Radio Emission of The Quiet Sun.

[8] Low Noise Block Down converter http://www.satsig.net/

Bulletin of Physics Projects

Design and Development of a Smartphone Based Visible Spectrophotometer for Analytical Applications

Bedanta Kr. Deka, D. Thakuria, H. Bora and S. Banerjee[#]

Department of Physicis, B. Borooah College, Ulubari, Guwahati-781007, Assam, India

[#]Corresponding author's e-mail address: somikbnrj@gmail.com

Abstract

The paper reports the design and development of a portable, low cost smartphone based spectrophotometer for analytical purpose. By integrating readily available laboratory optical components to the camera of a smartphone a spectrophotometer is designed. The image processing has been done with the imageJ software which gives the intensity vs. pixel curve. To get the intensity vs. wavelength curve a calibration is done with the help of color filters which works as monochromators. With the calibrated device spectroscopical analysis can be done. We envision that our designed sensor could emerge as a low cost, portable sensor with which spectroscopic analysis could be done.

1. Introduction

Measurement of the absorption spectrum of a sample plays a vital role in different fields of application that includes environmental and biological science, cosmology and various industrial applications. The contemporary methods used to measure and analyze this absorption spectrum of the sample are bulky and complex. There is a need to develop a simple portable UV-visible spectrophotometer which utilizes something which is as easily available as a smart phone camera and then interpret the results with a open source software. Currently it is estimated that there are over 2.5 billion smart phones in use which are equipped with advanced multi-dimensional features like wi-fi, Bluetooth, ambient light sensor, good mega-pixel cameras, accelerometer and many more. Also *i*-tunes and Google Play Store offer a rich variety of apps, which can be easily downloaded and take seconds to install. Considering the current scenario, researchers around the world are actively engaged in developing different types of smart phone based optical and electrochemical devices. In most cases camera of smart phone has been extensively utilized for developing different optical sensing tools, of which UV-visible spectroscopy is one.

Absorption spectroscopy refers to spectroscopic techniques that measure the absorption of radiation, as a

function of frequency or wavelength, due to its interaction with a sample. Absorption spectroscopy is performed across the electromagnetic spectrum. A material's absorption spectrum is the fraction of incident radiation absorbed by the material over a range of frequencies. The absorption spectrum is primarily determined[1][2][3] by the atomic and molecular composition of the material. Radiation is more likely to be absorbed at frequencies that match the energy difference between two quantum mechanical states of the molecules. The absorption that occurs due to a transition between two states is referred to as an absorption line and a spectrum is typically composed of many lines. The frequencies where absorption lines occur, as well as their relative intensities, primarily depend on the electronic and molecular structure of the sample. The frequencies will also depend on the interactions between molecules in the sample, the crystal structure in solids, and on several environmental factors (e.g., temperature, pressure, electromagnetic field).

The instrument used in ultraviolet-visible spectroscopy is called a UV-Visible spectrophotometer. It measures the intensity of light passing through a sample (I), and compares it to the intensity of light before it passes through the sample (I0). The ratio I/I0 is called the transmittance, and is usually expressed as a percentage (%T). The absorbance is based on the transmittance:

$$\text{Absorbance} = \log (I_0/I)$$

Absorption spectroscopy is employed as a tool to determine the presence of a particular substance in a sample and, in many cases, to quantify the amount of the substance present. Infrared and ultraviolet-visible spectroscopes are particularly common in analytical applications. Absorption lines are typically classified by the nature of the quantum mechanical change induced in the molecule or atom. Rotational lines, for instance, occur when the rotational state of a molecule is changed. Rotational lines are typically found in the microwave spectral region. Vibration lines correspond to changes in the vibration state of the molecule and are typically found in the infrared region. Electronic lines correspond to a change in the electronic state of an atom or molecule and are typically found in the visible and ultraviolet region. X-ray absorptions are associated with the excitation of inner shell electrons in atoms. These changes can also be combined (e.g. rotation-vibration transitions), leading to new absorption lines at the combined energy of the two changes.

In contemporary UV-visible spectrometer, the detector is typically a photomultiplier tube, photodiode or a photodiode array. Many detectors are grouped into one or two dimensional arrays and they are able to collect light of different wavelengths on different pixels or group of pixels simultaneously. Here the single photodiode detectors or photomultiplier tubes are used with scanning monochromator, so that its intensity may be measured as function of wavelength.

Smart phone cameras consist of lens and the sensor. The sensor that actually captures the image is a complex integrated circuit, which typically includes photo detectors, transistors and often some form of processing hardware and power management in a very compact manner. In the sensor, photo detectors corresponding to each pixel in the image capture analog information about the photons hitting them. This information gets amplified and converted into a digital signal relating to the brightness. The introduction section should briefly describe the background of the work with a brief literature survey on the topic. Recent developments in the field must also be clearly stated with proper references. The references cited in the text must be written inside a pair of third brackets in the manner shown [1].

2. Experimental Details

2.1. Spectrometer design and Operation

The schematic diagram of the proposed sensor is shown in the figure 1. Light signal from a white LED source is allowed to pass through a pinhole. The light rays then pass directly to the sample kept in a quartz cuvette or through a color filter depending on whether we are taking a direct photograph or one using a particular wavelength. The color filters used in the present work are Red with wavelength centered around 690nm, Green with that around 530nm and blue with wavelength centered around 470nm. The light beams then pass through a transmission grating before falling on the lens of the smart phone camera. The transmission grating has 15,000 lines per inch and it is used to disperse the beam into its constituent components. This entire arrangement is enclosed in a steel box which prevents light from outside falling on the lens of the camera as shown in figure 2. The box is painted

with a non reflective coating of black paint so that no light gets scattered from the walls of the box.
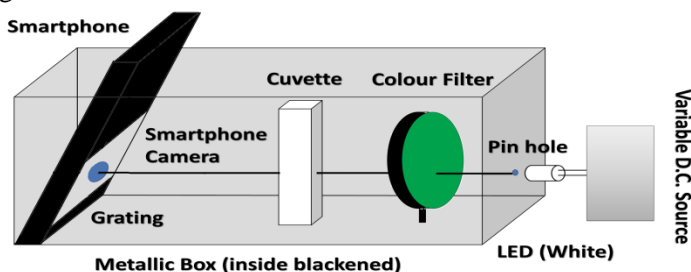
Fig. 1 Schematic Diagram of the visible spectrometer

If not checked that would interfere with the light coming from the sample. While making the arrangement special care is taken so that the pinhole, the color filter, the cuvette, the grating and the camera are aligned at same optical level. An arrangement is also made so that the smart phone and hence the camera can be rotated along a horizontal axis as it helps us focusing on the first and second order diffraction which are formed either below or above the light beam incident on the camera. Before taking the image the smart phone camera is locked at auto focus mode and the timer is set in the camera. The lead is closed and after the stipulated time, the phone takes the photo and the process is repeated again.

Fig. 2. Portable Visible Spectrophotometer as designed

2.2. Methodology

First a direct photo of the white light is taken after allowing the light to pass directly to the camera lens through the grating. The camera is arranged in such a way that it focuses on the 1st order diffraction maxima. The colour filters are introduced in front of the white LED and

without disturbing the previous arrangement photographs are taken. The sample is introduced in between the light source and the smartphone modified with grating and direct photographs of the sample are taken.

2.3. Data Acquisition and Analysis

The photos taken with help of the smart phone are transferred to a computer with a help of data cable and is then analyzed with a help of imageJ software, which is an image processing software developed by the National Institute of Health (NIH); USA. The software can sense the intensity in pixel columns and then plot intensity versus pixel curve. But to do spectroscopic analysis we need an intensity vs. wavelength curve and for that we need to do a calibration between wavelength and pixel that is achieved with the help of the images obtained using the monochromatic filters.

3. Results and Discussions

3.1. Image Processing and Device Calibration

The photos taken are processed with the imageJ software which converts them to spectral images. Firstly, a photo of the 1st order diffraction pattern of the white LED is taken with the smartphone camera using the above mentioned set-up. Applying imageJ the graph between transmitted intensity and pixels is plotted and is shown in the figure 3. With imageJ we plot the intensity vs. pixel curve for these photos as well which are also shown in the figure 3.
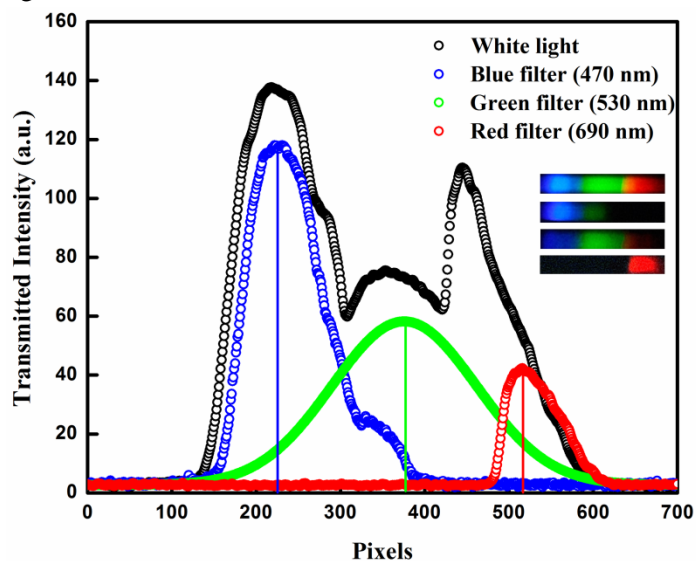
Fig. 3: Intensity vs. Pixel graphs for the 1st order Diffraction patterns from White LED and from the White LED after introduction of the colour filters

After that we take the photos of the 1st order diffraction patterns by introducing colour filters which works as monochromators and allows only a particular wavelength or a range of particular wavelengths to pass through. In the inset of Fig. 3, the real time diffraction patterns as captured by the smartphone camera are also shown.

The imageJ software can only plot the intensity versus pixel curve. But in order to do spectroscopic analysis we need to see the variation of intensity with wavelength. So the device needs to be calibrated accordingly. In order to do the calibration we took the photos with the help of filters. The approximate wavelength of the filter is known and as such a calibration curve between wavelength and pixels can be easily obtained. The pixel corresponding to which we get the highest intensity is taken for a particular wavelength range. So we get a coordinate of pixel with the corresponding wavelength. If we repeat the process for various filters we get the wavelength versus pixel calibration graph as shown in the Fig. 4.
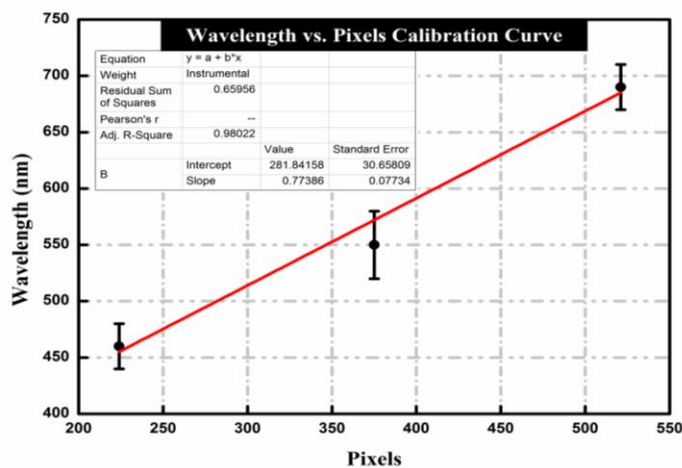
Fig. 4: Calibration Curve for the spectrophotometer

From the calibration curve that is linearly fitted with a regression co-efficient of 0.98, we can easily obtain a relation between the wavelength (λ) and pixel (p) that is given by:

$$\lambda = 281.8 + 0.77 \times p$$

Using the above equation the pixels as obtained from Image J software can be converted into wavelength and absorption spectra can be obtained.

3.2. Sample Analysis

For comparison of the smart-phone based visible spectrometer with an analytical spectrometer, the absorption spectra of $NiCl_2$ solution was investigated. With imageJ intensity vs. pixel curve was obtained and with the help of the equation obtained from the calibration curve, the corresponding intensity vs. wavelength curve was plotted as shown in the Fig. 5. However, the transmittance was converted into absorbance spectra for this purpose. The result is compared to the absorption spectra of $NiCl_2$ obtained from a Cary 60 UV-Visible spectrometer and plotted in the same graph below (Fig.5).
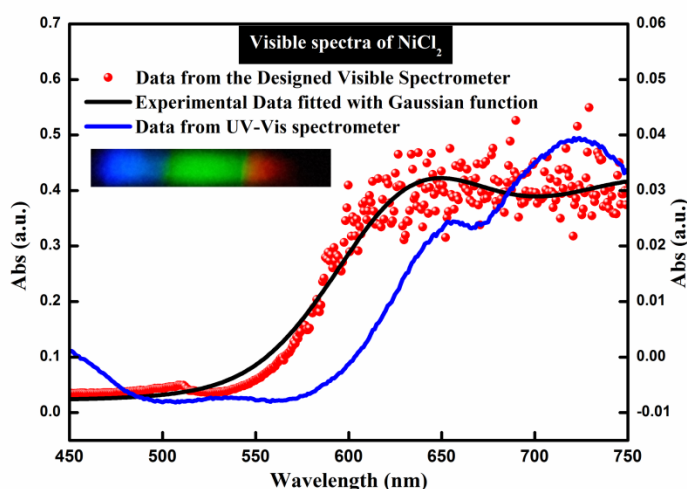
Fig. 5: Absorption spectra of $NiCl_2$ using UV-Visible and smart-phone based sensors

It is evident from the figure 5 that both the absorption spectra show reasonably good agreement with two peaks observed in the region from 600 to 750 nm. In order to find out the exact peak wavelengths both the absorption spectra were de-convoluted and are shown in figure 6 (a, b).From figure 6(a) the peaks are obtained at around 640nm and at 750 nm which is in agreement with the data obtained from the UV-Visible spectrometer [Fig. 6(b)]. The matching of the data from the two equipments clearly indicates that the portable visible spectrophotometer works effectively to obtain the absorption spectrograph of different chemicals. A portable visible spectrophotometer can be of tremendous use in the scientific field. Visible spectroscopy can determine transmittance, absorbance and reflectance of a sample in the visible range. Definite absorption spectrum in the visible range of a sample

indicates the presence of specific molecules or components in the sample solution.
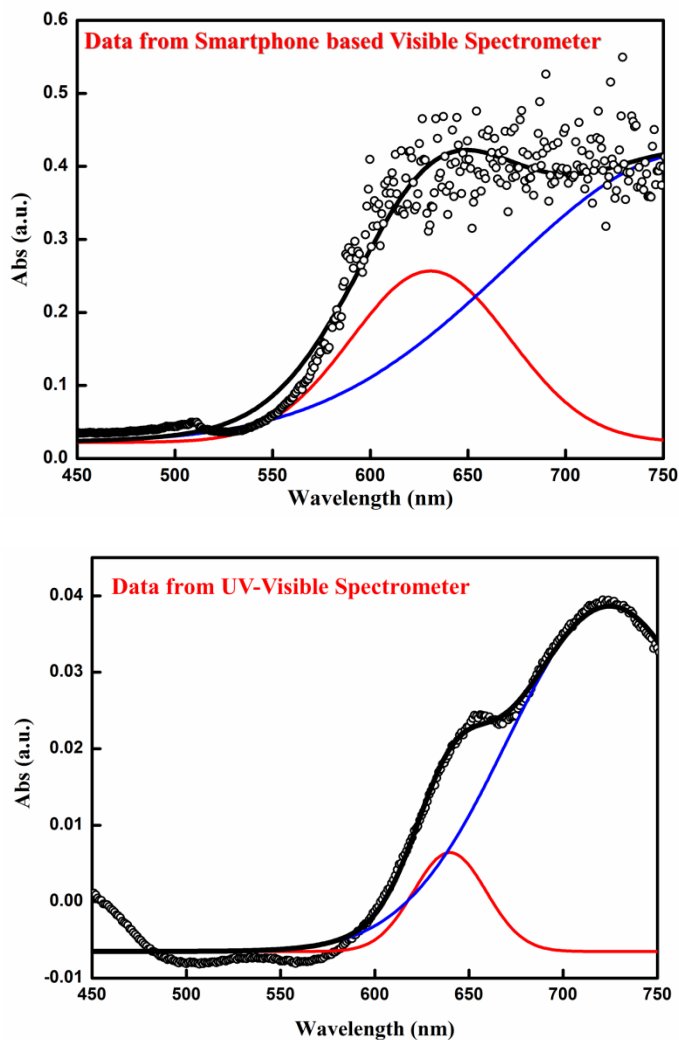
Fig. 6: De-convoluted spectra of (a) Smartphone based Visible spectrometer and (b) UV-Visible Spectrometer

4. Conclusions

The wavelength of absorption peaks can be correlated with the types of bonds in a given molecule and are valuable in determining the functional groups within a molecule. The concentration of the sample solution can also be obtained from the absorbance(A) using Beer-Lambert law given by:

$$A = \varepsilon \, l \, c$$

where, ε is molar absorption coefficient of the solution, l is the length of the cuvette, c is the molar concentration of the solution. Concentration measurements lead us to know about purity of the substance, rate constants of chemical reactions etc. Visible spectroscopy can also be used for many industrial purposes.

In order to make the instrument portable and inexpensive certain tradeoffs have to be made. In a traditional spectrometer we can do real time analysis of the direct intensity I and the intensity we get after the light passes through the sample. Also the filters have to be placed manually in the spectrometer while the traditional one uses an automatic arrangement. All these may introduce some error in the final result. The color filters used during the calibration allows a range of wavelengths to pass through them instead of a single wavelength which may lead to some error in the calibration curve.

5. Acknowledgement

6. References

[1] Absorption spectroscopy (https://en.m.wikipedia.org)
[2] UV-visible spectroscopy (https://en.m.wikipedia.org)
[3] Smart phone camera (https://www.techspot.com)
[4] Using UV-visible spectrum to identify samples (https://www.chemguide.co.uk)
[5] Global mobile statistics (https://www.statista.com)